



AFRL-RY-WP-TR-2012-0299

**HIGH-EFFICIENCY AND HIGH-POWER MID-WAVE
INFRARED CASCADE LASERS**

**Claire Gmachl
Trustees of Princeton University**

**OCTOBER 2012
Final Report**

Approved for public release; distribution unlimited

**AIR FORCE RESEARCH LABORATORY
SENSORS DIRECTORATE
WRIGHT-PATTERSON AIR FORCE BASE, OH 45433-7320
AIR FORCE MATERIEL COMMAND
UNITED STATES AIR FORCE**

NOTICE AND SIGNATURE PAGE

Using Government drawings, specifications, or other data included in this document for any purpose other than Government procurement does not in any way obligate the U.S. Government. The fact that the Government formulated or supplied the drawings, specifications, or other data does not license the holder or any other person or corporation; or convey any rights or permission to manufacture, use, or sell any patented invention that may relate to them.

This report is the result of contracted fundamental research deemed exempt from public affairs security and policy review in accordance with SAF/AQR memorandum dated 10 Dec 08 and AFRL/CA policy clarification memorandum dated 16 Jan 09. This report is available to the general public, including foreign nationals.

Copies may be obtained from the Defense Technical Information Center (DTIC)
(<http://www.dtic.mil>).

AFRL-RY-WP-TR-2012-0299 HAS BEEN REVIEWED AND IS APPROVED FOR PUBLICATION IN ACCORDANCE WITH ASSIGNED DISTRIBUTION STATEMENT.

*//Signature//

MATT GRUPEN, Project Manager
EO/IR Sensing Technology Branch
Aerospace Components Division

//Signature//

THOMAS R. NELSON, Chief
EO/IR Sensing Technology Branch
Aerospace Components Division

//Signature//

BRADLEY CHRISTIANSEN, Deputy
Aerospace Components Division
Sensors Directorate

This report is published in the interest of scientific and technical information exchange, and its publication does not constitute the Government's approval or disapproval of its ideas or findings.

*Disseminated copies will show “//Signature//” stamped or typed above the signature blocks.

REPORT DOCUMENTATION PAGE				<i>Form Approved OMB No. 0704-0188</i>	
<p>The public reporting burden for this collection of information is estimated to average 1 hour per response, including the time for reviewing instructions, searching existing data sources, gathering and maintaining the data needed, and completing and reviewing the collection of information. Send comments regarding this burden estimate or any other aspect of this collection of information, including suggestions for reducing this burden, to Department of Defense, Washington Headquarters Services, Directorate for Information Operations and Reports (0704-0188), 1215 Jefferson Davis Highway, Suite 1204, Arlington, VA 22202-4302. Respondents should be aware that notwithstanding any other provision of law, no person shall be subject to any penalty for failing to comply with a collection of information if it does not display a currently valid OMB control number. PLEASE DO NOT RETURN YOUR FORM TO THE ABOVE ADDRESS.</p>					
1. REPORT DATE (DD-MM-YY) October 2012		2. REPORT TYPE Final		3. DATES COVERED (From - To) 1 February 2007 – 12 May 2012	
4. TITLE AND SUBTITLE HIGH-EFFICIENCY AND HIGH-POWER MID-WAVE INFRARED CASCADE LASERS				5a. CONTRACT NUMBER FA8650-07-1-7708	
				5b. GRANT NUMBER	
				5c. PROGRAM ELEMENT NUMBER 62702E	
6. AUTHOR(S) Claire Gmachl				5d. PROJECT NUMBER ARPR	
				5e. TASK NUMBER ND	
				5f. WORK UNIT NUMBER YOKS	
7. PERFORMING ORGANIZATION NAME(S) AND ADDRESS(ES) Trustees of Princeton University Office of Research and Project Administration 1 Nassau Hall Princeton, NJ 08544-0001				8. PERFORMING ORGANIZATION REPORT NUMBER AFRL-RY-WP-TR-2012-0299	
9. SPONSORING/MONITORING AGENCY NAME(S) AND ADDRESS(ES) Air Force Research Laboratory Sensors Directorate Wright-Patterson Air Force Base, OH 45433-7320 Air Force Materiel Command United States Air Force		Defense Advanced Research Projects Agency (DARPA/DSO) 675 North Randolph Street Arlington, VA 22203-2114		10. SPONSORING/MONITORING AGENCY ACRONYM(S) AFRL/RYPD	
				11. SPONSORING/MONITORING AGENCY REPORT NUMBER(S) AFRL-RY-WP-TR-2012-0299	
12. DISTRIBUTION/AVAILABILITY STATEMENT Approved for public release; distribution unlimited.					
13. SUPPLEMENTARY NOTES Report contains color.					
14. ABSTRACT This report summarizes advanced quantum cascade laser (QCL) development during the Phase Ib performance period of DARPA's EMIL program. Examining tunneling in QCLs, we found that strong dephasing from interface roughness scattering poses a likely bottleneck for electron transport. We therefore proposed an "ultra-strong coupling design" strategy and calculated the optimal coupling strength with a density matrix based model. By implementing the ultra-strong coupling design strategy in real QCLs, we demonstrated a major step forward in the overall device performance and achieved a record breaking wall plug efficiency (WPE) of ~50% (pulsed at cryogenic temperatures). Ultra-strong coupling also produced QCLs with exceedingly broad optical gain (e.g. > 400 cm ⁻¹ at peak emission wavelengths around 4.x μm), as well as low threshold current density, large slope efficiency (~5 W/A), and high WPE (~23 %) in pulsed mode at 295 K. To further study transport in QCLs, electron transit times of different QCLs were measured and compared to calculated upper laser level lifetimes with and without interface roughness scattering. A better correlation is found when including interface roughness, suggesting that it plays a crucial role in determining intersubband lifetimes in mid-infrared QCLs and should routinely be included in design.—See next page for alternate Abstract.--					
15. SUBJECT TERMS mid-infrared; strong coupling injection; superlattice tunneling; quantum cascade laser; interface roughness scattering					
16. SECURITY CLASSIFICATION OF:			17. LIMITATION OF ABSTRACT: SAR	18. NUMBER OF PAGES 76	19a. NAME OF RESPONSIBLE PERSON (Monitor) Matt Grupen 19b. TELEPHONE NUMBER (Include Area Code) N/A
a. REPORT Unclassified	b. ABSTRACT Unclassified	c. THIS PAGE Unclassified			

14. Abstract, cont.

Quantum Cascade (QC) lasers have seen and continue to see rapid performance improvements driven by applications such as chemical trace gas sensing or infrared countermeasures. The DARPA EMIL program has contributed immeasurable value to the development of high-performance QC lasers, especially in the short 4 – 5 μm wavelength range. High wall-plug efficiency (WPE) was one of this program's main focus. This report summarizes our team's main activities and results during the Phase Ib performance period.

We examined the major electron transport processes in QC lasers and studied in depth the resonant tunneling process. We have found that due to the strong dephasing in connection with the interface-roughness-induced intrasubband scattering, the resonant tunneling process between the injector ground state and the downstream upper laser state is likely the bottleneck for the electron transport through the device. Such an interface-roughness-induced dephasing effect was long underestimated in conventional QC laser design, that the coupling strength employed in most conventional QC laser designs was not sufficient to effectively overcome its negative influence on the resonant tunneling process. Therefore, we have proposed to employ a much larger coupling strength in QC laser band-structure designs which we refer to as the **“ultra-strong coupling design”** strategy, and calculated the optimal coupling strength with our density matrix based model.

By implementing the ultra-strong coupling design strategy in real QC lasers, we have demonstrated a major step forward in the overall device performance and achieved a record breaking QC laser WPE of ~50% (operated in pulsed mode at cryogenic temperatures).

In addition, the ultra-strong coupling design strategy has been applied to realization of QC lasers with exceedingly broad optical gain. QC laser structure was demonstrated that provide a broadband gain spectrum of $> 400 \text{ cm}^{-1}$ at peak emission wavelengths around $4.x \mu\text{m}$. Low threshold current densities, large slope efficiency (up to $\sim 5 \text{ W/A}$) and high wall plug efficiency (up to $\sim 23 \%$) were achieved in pulsed mode operation at 295 K.

We have further explored different design strategies combined with the ultra-strong coupling to effectively improve the temperature performance of these QC lasers.

Finally, to further study the importance of interface-roughness scattering on QC lasers, we examined the transport characteristics of QC lasers in a brief meta-study. The electron transit time of many different QC lasers has been measured and compared to the calculated upper laser level lifetimes with and without taking into account interface-roughness-induced intersubband scattering. A significantly better correlation is found between the experimental results and the calculation when including the contribution from the interface roughness (corr. coeff.: 0.79 vs. 0.43 with and without the consideration of interface roughness, respectively). This suggests that in addition to longitudinal optical phonons, interface roughness is also crucial in determining the intersubband lifetimes in mid-infrared QC lasers, and should routinely be included in design.

This, in turn, provides guidance for future QC laser design.

Table of content

Abstract	ii
Table of Content	iii
List of Tables	iv
List of Figures	v
Acknowledgement	ix
1 Introduction	1
1.1 Preamble	1
1.1.1 Anticipated tasks	1
2 High-performance Quantum Cascade Lasers Employing Ultra-strong Coupling Design Strategy	2
2.1 WPE of QC lasers	2
2.2 Electron transport in QC structures	10
2.3 Role of interface roughness in key resonant tunneling processes	15
2.4 Optimization of the coupling strength	17
2.5 High performance QC lasers employing ultra-strong coupling design strategy	22
2.5.1 Band-structure design	22
2.5.2 Waveguide structure design	25
2.5.3 Device fabrication	26
2.5.4 Device characterization results	28
2.6 Ultra-strong coupling QC lasers with broad-band optical gain	36
2.6.1 Band-structure design	36
2.6.2 Waveguide structure design	38
2.6.3 Device characterization results	38
2.7 Influence of taller electron exit barriers on the temperature performance of ultra-strong coupling QC lasers	43
2.7.1 Band-structure design	44

2.7.2	Device characterization results	45
2.8	Conclusions and discussions	49
2.9	Summary of the Ultra-strong Coupling QC Lasers	54
3	Importance of interface roughness induced intersubband scattering in mid-infrared Quantum Cascade lasers	55
4	References	59

List of Tables

1	Summary of the 12 ultra-strong coupling QC designs and some characterization results	53
2	Summary of the laser characterization results of the 12 ultra-strong coupling QC designs	54

List of Figures

2.1	Schematic of the periodic 3-level laser system model for describing a typical QC laser	5
2.2	Light-current-voltage (LIV) characteristics for a typical QC lasers	10
2.3	STM image of a superlattice structure	11
2.4	Schematic of the interface roughness induced elastic intersubband scattering process	12
2.5	Schematic of the periodic two-level system model for studying the resonant tunneling process through the thick injection barrier in QC lasers	14
2.6	Schematic of the density matrix model based on a periodic three-level system.	19
2.7	The trend of the peak optical gain as a function of the coupling strength Ω_c	22
2.8	Band-structure of one of the best performing ultra-strong coupling QC laser designs (wafer No. A785)	23
2.9	Band-structure of the same design in Fig. 2.8 with the localized wavefunctions in the divided bases plotted	24
2.10	Waveguide structure design for wafer A785 and the transverse mode profile	25
2.11	Profiles of the material composition elements, the silicon dopant and other impurity atoms in the epitaxial layers characterized with SIMS	27
2.12	(a) Optical microscope image of a packaged ridge waveguide QC laser chip. (b) SEM image of a QC laser as-cleaved facet	27
2.13	Spectra of the EL of a mesa sample at 80 K and 300 K	28
2.14	IV characteristics for a non-lasing mesa sample at 80 K and 300 K	29
2.15	Comparisons of electron transport properties (IV characteristics) of the ultra-strong coupling design and an exemplary conventional design of similar wavelength ($\sim 4.7 \mu\text{m}$ at 80 K) at 80 K (a) and at 300 K (b)	29
2.16	Representative laser spectra at 80 K and 300 K	30
2.17	(a) Pulsed LIV measurements for an as-cleaved $13.6 \mu\text{m}$ wide, 2.9 mm long QC laser at various heat sink temperatures as indicated. (b) The WPE versus current is extracted from the measurement results in (a)	31

2.18	Far-field measurements of the laser beam profiles along the growth direction and the in-plane direction	31
2.19	Scatter plot of pulsed-mode peak WPE at 80 K for all tested lasers with various cavity lengths	32
2.20	Waveguide loss measurement at 80 K with “1/L” method	33
2.21	Extraction of the characteristic temperature T_0 from the threshold current density vs. operating temperature plot	33
2.22	(a) CW LIV characteristics for the same laser shown in Fig. 2.17 at heat-sink temperatures of 30 K and 80 K. (b) The CW WPE versus current extracted from the results in (a)	34
2.23	(a) Pulsed LIV characteristics for a buried-heterostructure QC laser (14 μm wide and 1.9 mm long) with back-facet HR coating at various heat-sink temperatures. (b) The pulsed WPE versus current extracted from the experimental results in (a)	35
2.24	(a) CW LIV characteristics for the same laser in Fig. 2.23 at various heat-sink temperatures. (b) The CW WPE versus current extracted from the experimental results in (a)	35
2.25	Band-structure of the broad-band optical gain ultra-strong coupling QC laser design (wafer No. A1392)	37
2.26	Band-structure of the same design in Fig. 2.25 with the localized wavefunctions in the divided bases plotted	37
2.27	Waveguide structure design for wafer A1392 and the transverse mode profile	39
2.28	(a) EL spectra measured from a half-circular mesa operated at 1 kA/cm^2 current density and various temperatures. (b) FWHM of the EL spectra at various operating temperatures and the percentage of the transition energy they correspond to	39
2.29	IV characteristics for a circular non-lasing mesa at various operating temperatures	40
2.30	Representative laser spectra at 80 K and 300 K	41
2.31	(a) Pulsed LIV characteristics for a representative QC laser (3 mm long and 16.3 μm wide ridge) at various heat-sink temperatures. (b) WPE calculated from the experimental results in (a)	41
2.32	Characteristic temperature T_0 (~ 107 K) extracted from the threshold current	42

	versus operating temperature plot	
2.33	Waveguide loss at 80 K extracted with the “1/L” method	42
2.34	Band-structures for the pair of two-LO-phonon designs	45
2.35	Band-structures for the pair of three-LO-phonon designs	45
2.36	EL spectra for the two-LO-phonon baseline design (top) and the two-LO-phonon taller-barrier design (bottom) at 80 K and 300 K	46
2.37	EL spectra for the three-LO-phonon baseline design (top) and the three-LO-phonon taller-barrier design (bottom) at 80 K and 300 K	47
2.38	Representative QC laser LIV characteristics for the two-LO-phonon baseline design (a) and the taller-barrier design (c), together with the extracted characteristic temperatures (b) and (d)	48
2.39	Representative QC laser LIV characteristics for the three-LO-phonon baseline design (a) and the taller-barrier design (c), together with the extracted characteristic temperatures (b) and (d)	49
2.40	Illustration of the definition of ΔE , the energy difference between the upper laser states (red curves) and the band edge of the lowest satellite valleys of the quantum well material (orange dashed line)	51
2.41	(a) Correlation plot for modal gain coefficient versus $1/(L_p \cdot \gamma_{32})$. (b) Correlation plot for modal gain coefficient versus ΔE . (c) Correlation plot for modal gain coefficient versus $\Delta E/(L_p \cdot \gamma_{32})$	52
2.42	(a) Plot of output optical power, WPE and lateral far-field divergence angle versus input current for one of the highest performance ultra-strong QC lasers (from wafer A785). (b) Lateral far-field profiles at several different input current values for the same laser in (a)	53
3.1	Typical band structure of a QC laser with upper laser level in red, lower laser level in blue and injector state in green. The parabolas represent the energy dispersion for each subbands with the arrow indicating the interface roughness induced transition from the upper to lower laser levels.	54
3.2	Upper laser level lifetimes and (b) lower laser level lifetimes calculated for different QC laser designs. Black squares are lifetimes calculated by IFR scattering only. Red circles are lifetimes calculated by LO phonon scattering only. Blue triangles are lifetimes taking into account of both IFR and LO phonon scattering. Different color shaded area represent different lasing wavelength regions.	55

3.3	Calculated upper laser level lifetimes when both LO-phonon and IFR scattering are taken into account as a function of wavelength. The dashed line is a guide for the eye only.	56
3.4	Current-voltage characteristic of a non-lasing circular mesa sample at T=80 K. The inset shows the light-current-voltage characteristic of a laser fabricated from the same wafer.	57
3.5	Measured transit lifetimes as a function of the lasing wavelength. Different shapes (colors) indicate different growth facilities and growth techniques.	57
3.6	Blue triangles and red circles are the calculated upper laser level lifetimes plotted as a function of half the measured transit lifetimes with and without taking into account of interface roughness scattering, respectively. The lines are linear fits through the data points. The inset table lists the slopes, standard error and correlation coefficients of the fit curves.	58

Acknowledgement

I would like to acknowledge the exceptional teamwork and outstanding contributions of all members of our team at AdTech Optics, Daylight Solutions, Johns Hopkins University, the Naval Research Labs, and Princeton University. My special thanks goes out to our graduate and undergraduate students as well as post-doctoral researchers involved in this project. Many nights spent in the labs and on the computers served not only to raise the performance of QC lasers to new heights, but they also influenced your future careers.

I would like to thank Dr. Thomas R. Nelson and Dr. Matthew E. Grupen and their staff for checking in on us always with encouragement and always seeing and pointing out the positive aspects of our work. Their positive guidance and intelligent questions proved invaluable many times over. I would like to also acknowledge our managers at DARPA, Dr. Mark Rosker, in particular, and his collaborators on the EMIL project, including the teams conducting the review meetings. Their constant challenges and interesting questions proved most useful and enlightening. The results of the EMIL program would not have reached the level they did if not for their untiring behind-the-scenes work.

I would also like to acknowledge our competing teams in the EMIL program. We have shared more insights and data with each other than will ever be known publicly, and the fairness and excitement in pursuing a common goal was most enjoyable.

Finally, posthumously, my heart-felt gratitude to Dr. Henryk Temkin, who started the EMIL program so strongly and led it far longer than his illness seemingly allowed it. His dedication to his projects was most palpable, and in this he inspired many of us to work harder and more sincerely. He will be missed.

1. Introduction

1.1. Preamble “*Ultra-strong coupling Quantum Cascade lasers*”

The DARPA EMIL Phase 1b work presented in this report is a follow-on to our team’s Phase 1 results that led to the first 50% efficient (in pulsed mode at cryogenic temperatures) Quantum Cascade (QC) lasers. This was achieved with the new design of so-called “ultra-strong coupling QC lasers”. At the end of Phase 1, it was noted that our understanding of the electron transport process in QC lasers, especially from the injector into the upper laser level, albeit already improved in the ultra-strong coupling QC lasers, was still incomplete. In the ensuing reporting period, we have greatly improved on our understanding of this transport process, and the importance of interface-roughness scattering for transport.

The improved transport process has immediate beneficial impact on various aspects of the wall-plug efficiency (WPE):

- (i) The *internal efficiency* increases as fewer electrons scatter into states other than the upper laser states.
- (ii) The *current efficiency* increases as the differential resistance is reduced and a higher current can be carried by the structure for the same amount of doping.
- (iii) The *voltage efficiency* is unchanged (i.e. not diminished over other approaches), as the injection process is independent of applied field and injector energy drop.
- (iv) The *optical efficiency* should not be affected or should potentially improve as less doping can be used.

1.1.1. Anticipated tasks

Phase 1b was then dedicated to further explore, optimize, and adapt the ultra-strong coupling design for the overall improvement of QC lasers operating in continuous wave mode and at room temperature. In particular:

1. For the optimization of the strong-coupling injection scheme, the coupling for the parameters of input coupling strength, doping density, and exit coupling strength was subject to study and optimization.
2. For continuous-wave and/or room-temperature operation, the voltage defect and backfilling processes needed to be studied and optimized, while retaining strong coupling.

3. As the amount of optimum strong-coupling depends on the interface roughness of the wells and barriers of the injector/active region interface, the roughness needed closer study.
4. For the optimization of the optical efficiency, the optical loss needed re-evaluation and – as far as possible – reduction.

In the following, we are first providing a general background to the improved understanding of ultra-strong coupling QC lasers; followed by in-depth discussions of interface roughness and its import for QC lasers. The first text follows Chapter 2 in a recently completed Ph.D. thesis by Peter Q. Liu in the PI's group at Princeton University, and the remainder follows several publications by team members. Excess wafer material from this study has furthermore been used in studies of single-mode QC lasers, which we briefly discuss at the end of this report.

2. High-performance Quantum Cascade Lasers Employing Ultra-strong Coupling Design Strategy

For most QC laser based applications, it is highly desirable that the QC lasers can be operated without complicated and bulky cooling systems while still providing sufficient optical power. The demand on the capacity of the cooling systems mainly depends on the total power consumption of the QC lasers. Therefore, to meet such a goal the QC lasers need to be highly power-efficient, especially for applications where high optical power is another prerequisite. For a real QC laser, its power-efficiency, also known as WPE (acronym for wall-plug efficiency as denoted in Chapter 1), is determined by several factors: the intrinsic characteristics associated with the band-structure [1-3] and the waveguide structure designs [4], the epitaxial growth quality [5], and the quality of device fabrication and packaging processes. The factor associated with the structure designs is of distinctive importance in the sense that it determines the ultimate device performance that can be achieved, and it is expected to have plentiful potential for further improvement. Moreover, it also appears to be an interesting research topic in an academic setting. Therefore, our efforts on advancing the QC laser overall performance with an emphasis on WPE substantially focus on explorations and optimizations from the design perspective.

2.1 WPE of QC lasers

In order to improve the performance of QC lasers, especially the WPE, it is necessary to conduct a thorough study on which crucial device parameters determine the WPE [6,7] and how to further improve them to benefit the WPE. The WPE of a QC laser characterizes the efficiency of the conversion from the device input electric power into its output optical power.

The input electric power (P_{in}) equals the product of the input current (I) and the applied voltage (V) across the device:

$$P_{in} = I \cdot V . \quad (2.1)$$

The total applied voltage on the device contains two parts:

$$V = V_{core} + V_p \quad (2.2)$$

where V_{core} is the voltage applied to the active core of the QC laser, and V_p is the parasitic voltage drop across the metal contacts and the waveguide cladding layers. If we assume the electric field is uniform across the entire laser active core, then V_{core} is the product of the voltage drop across each pair of the active region/injector (ΔV) and the number of such pairs (N):

$$V_{core} = N \cdot \Delta V \quad (2.3)$$

It can be easily seen from the band-structure of an operating QC laser that $\Delta V \cdot e$, where e is the charge of the electron, equals the sum of the photon energy (E_{ph}) and the energy defect (E_{def}), i.e. the energy difference between the lower laser state and the upper laser state in the downstream active region:

$$\Delta V \cdot e = E_{ph} + E_{def} . \quad (2.4)$$

Both E_{ph} and E_{def} are determined by the active core design of the QC laser. The parasitic voltage drop V_p across the metal contacts and the waveguide cladding layers can be characterized by an effective parasitic resistance R_p :

$$V_p = I \cdot R_p . \quad (2.5)$$

Therefore, combining Eqns. (2.1)-(2.5), the input electric power P_{in} can be expressed as

$$P_{in} = I \cdot [N(E_{ph} + E_{def})/e + I \cdot R_p] . \quad (2.6)$$

To reveal the key factors for the output optical power of a QC laser (P_{out}), we make another assumption that the slope efficiency (S) of the QC laser above the laser threshold current (I_{th}) is constant, and therefore when the QC laser is operated above the threshold,

$$P_{out} = S(I - I_{th}) . \quad (2.7)$$

The remaining task is to write down the laser slope efficiency S in terms of the basic device parameters. The laser slope efficiency, which characterizes the amount of the output optical power increment as a result of a unit input current increment, consists of two factors: (1) the amount of optical power generated within the laser cavity due to a unit input current increment

and (2) the fraction of the generated optical power that eventually couples out of the laser cavity. Factor (1) is also known as the internal quantum efficiency (η_{int}) and factor (2) is usually called the optical extraction efficiency (η_{extr}). The optical extraction efficiency satisfies the expression

$$\eta_{extr} = \frac{\alpha_m}{\alpha_m + \alpha_w}, \quad (2.8)$$

where α_w is the waveguide loss associated with the laser cavity, and α_m is the mirror loss associated with the facets of the cavity which follows the conventional definition for a FP cavity

$$\alpha_m = \frac{-\ln(R_1 R_2)}{2n_{eff}L}, \quad (2.9)$$

where R_1 and R_2 are the mirror reflectivities for the front-facet and the back-facet, respectively, n_{eff} is the effective refractive index of the waveguide structure and L is the FP cavity length. The internal quantum efficiency involves more fundamental parameters corresponding to the microscopic processes of the device operation, nevertheless, it can be derived from the rate equations for QC lasers.

For realistic QC lasers, the band-structure for one period of the active region/injector pair typically consists of around 10 or more quantized energy subbands (states) involved in the radiative intersubband transition and the electron transport process, a large fraction of which are within the injector miniband. One can write down the rate equations for all the relevant states and take into account all the possible transitions. Such a set of rate equations is conceivably rather complicated. However, for all the different states in the injector miniband, the details of the interactions among themselves are not of particular interest for analyzing the radiative transition, therefore, when deriving parameters such as the internal quantum efficiency of a QC laser, the entire injector miniband can be treated as a single virtual state with corresponding effective transition lifetimes to account for its interactions with other states. In fact, the model for the band-structure of a QC laser can be further simplified by treating all the states between the lower laser state and the upper laser state in the downstream active region as one equivalent state without loss of accuracy for predicting the properties of the radiative process, such as the optical gain or the internal quantum efficiency. In this way, a periodic three-level laser system model describing a typical QC laser is constructed as illustrated in Fig. 2.1.

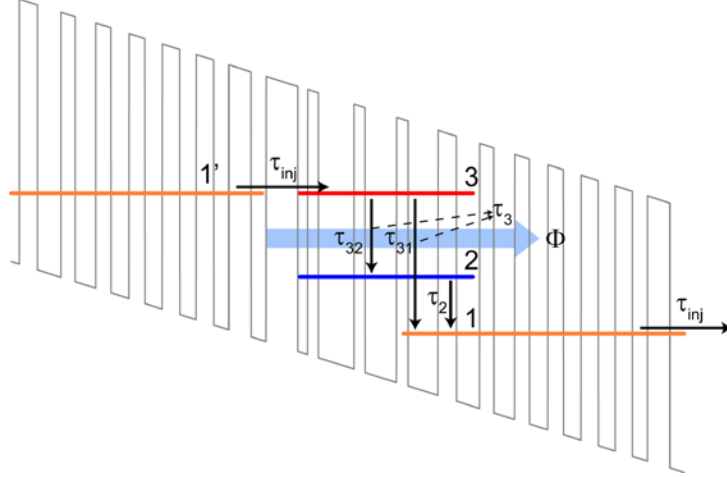


Fig. 2.1 Schematic of the periodic 3-level laser system model for describing a typical QC laser. Level 3 is the upper laser state, level 2 is the lower laser state, and level 1 is the equivalent injector state (level 1' is the equivalent injector state from the previous period). This model also assumes that non-radiative transitions take place between the following states: $3 \rightarrow 2$ with transition lifetime τ_{32} , $3 \rightarrow 1$ with transition lifetime τ_{31} (the upper laser state lifetime due to non-radiative relaxations is therefore $\tau_3 = \tau_{32}\tau_{31}/(\tau_{32} + \tau_{31})$), $2 \rightarrow 1$ with transition lifetime τ_2 , $1 \rightarrow 3$ in the downstream active region with transition lifetime τ_{inj} . The photon flux in the cavity is Φ .

For a QC design laser with N stages of active region/injector pairs and an active core mode confinement factor of Γ , we can further assume each stage has an average mode confinement factor Γ/N , which would be a good approximation when the thickness of the active core is smaller than or comparable to the wavelength. Based on the above 3-level laser system model and neglecting the influence from the environmental temperature, the rate equations for the electron populations in one period of active region/injector pair read:

$$\frac{dN_3}{dt} = \frac{N_1}{\tau_{inj}} - \frac{N_3}{\tau_3} - (N_3 - N_2) \cdot \sigma \cdot \frac{\Gamma}{N} \cdot \Phi, \quad (2.10)$$

$$\frac{dN_2}{dt} = \frac{N_3}{\tau_{32}} - \frac{N_2}{\tau_2} + (N_3 - N_2) \cdot \sigma \cdot \frac{\Gamma}{N} \cdot \Phi, \quad (2.11)$$

$$\frac{dN_1}{dt} = \frac{N_3}{\tau_{31}} + \frac{N_2}{\tau_2} - \frac{N_1}{\tau_{inj}}, \quad (2.12)$$

where N_1 , N_2 and N_3 are the electron populations on the states 1, 2 and 3, respectively, σ is the transition crosssection associated with the radiative intersubband transition between state 3 and state 2, all the lifetimes are explained in Fig. 2.1, and Φ is the photon flux in the cavity, and is given by

$$\Phi = \frac{N_{ph}}{V_{ph}} c, \quad (2.13)$$

where N_{ph} is the total number of photons in the cavity, V_{ph} is the mode volume of the photons, and c is the speed of light in the laser waveguide. In addition we have the conservation of total electron population

$$N_1 + N_2 + N_3 = N_{total} , \quad (2.14)$$

where N_{total} is the total electron population for one stage of active region/injector pair. The rate equation for the photon population is given by:

$$\frac{dN_{ph}}{dt} = N(N_3 - N_2) \cdot \sigma \cdot \frac{\Gamma}{N} \cdot \Phi - \frac{N_{ph}}{\tau_{ph}} , \quad (2.15)$$

where τ_{ph} is the photon lifetime associated with the cavity. To find the steady state solution for the above rate equations, one can set dN_1/dt , dN_2/dt , dN_3/dt and dN_{ph}/dt in Eqns. (2.10)-(2.12) and (2.15) all to be zero and solve for the desired parameters:

$$\frac{N_1}{\tau_{inj}} - \frac{N_3}{\tau_3} - (N_3 - N_2) \cdot \sigma \cdot \frac{\Gamma}{N} \cdot \Phi = 0 , \quad (2.16)$$

$$\frac{N_3}{\tau_{32}} - \frac{N_2}{\tau_2} + (N_3 - N_2) \cdot \sigma \cdot \frac{\Gamma}{N} \cdot \Phi = 0 , \quad (2.17)$$

$$\frac{N_3}{\tau_{31}} + \frac{N_2}{\tau_2} - \frac{N_1}{\tau_{inj}} = 0 , \quad (2.18)$$

$$(N_3 - N_2) \cdot \sigma \cdot \Gamma \cdot \Phi - \frac{N_{ph}}{\tau_{ph}} = 0 . \quad (2.19)$$

Also we notice that in the above equations, N_1 only appears in the form of N_1/τ_{inj} which corresponds to the current flowing through the structure

$$I = \frac{eN_1}{\tau_{inj}} . \quad (2.20)$$

Therefore, from Eqns. (2.16)-(2.20) and with the help of Eqn. (2.13) we can find the steady state solution for N_{ph} in terms of current I to be

$$\frac{N_{ph}}{\tau_{ph}} = N \frac{\tau_{32}\tau_3 - \tau_2\tau_3}{\tau_{32}\tau_3 - \tau_2\tau_3 + \tau_{32}\tau_2} \cdot \frac{I}{e} - N \frac{\tau_{31}V_{ph}}{\tau_3\tau_{ph}(\tau_{31} + \tau_2) \cdot \sigma \cdot \Gamma} . \quad (2.21)$$

The term N_{ph}/τ_{ph} in Eqn. (2.21) characterizes the number of photons lost within the cavity per unit time, which also equals the number of photons generated per unit time. Therefore the internal efficiency is derived as:

$$\eta_{int} = \frac{dP_{gen}}{dI} = \frac{d(N_{ph} \cdot E_{ph} / \tau_{ph})}{dI} = N \frac{\tau_{32}\tau_3 - \tau_2\tau_3}{\tau_{32}\tau_3 - \tau_2\tau_3 + \tau_{32}\tau_2} \cdot \frac{E_{ph}}{e}, \quad (2.22)$$

where P_{gen} denotes the total optical power generated within the cavity. The expression on the right hand side of Eqn. (2.22) can be rearranged as

$$\eta_{int} = N \frac{\tau_{32}\tau_3 - \tau_2\tau_3}{\tau_{32}\tau_3 - \tau_2\tau_3 + \tau_{32}\tau_2} \cdot \frac{E_{ph}}{e} = N \frac{\tau_{eff}}{\tau_{eff} + \tau_2} \cdot \frac{E_{ph}}{e}, \quad (2.23)$$

where τ_{eff} is defined as

$$\tau_{eff} = \tau_3 \left(1 - \frac{\tau_2}{\tau_{32}}\right). \quad (2.24)$$

The above expression for η_{int} allows one to estimate the output optical power with Eqn. (2.7). However, the model of the QC laser shown in Fig. 2.1 is rather idealized, because it assumes all the electrons from the injector are eventually injected onto the upper laser state, which can be quite different from reality. Besides being injected into the upper laser state, the electrons from the injector can also go through various leakage paths, such as being injected into the states above the upper laser state and subsequently relaxing down to the lower laser state, directly relaxing down to the lower laser state, or escaping into the continuum states via thermal excitation, etc. All of these leakage paths of electron transport contribute to the current flow through the structure but bypass the radiative transition, and thus lower the slope efficiency. In order to obtain a more accurate estimation of the slope efficiency, an important modification which takes into account the percentage of the electrons from the injector injected onto the upper laser state should be included in the internal quantum efficiency expression for QC lasers. This percentage is referred to as the electron injection efficiency η_{inj} here, and the modified internal quantum efficiency expression is then

$$\eta_{int} = \eta_{inj} \cdot N \frac{\tau_{32}\tau_3 - \tau_2\tau_3}{\tau_{32}\tau_3 - \tau_2\tau_3 + \tau_{32}\tau_2} \cdot \frac{E_{ph}}{e} = \eta_{inj} \cdot N \frac{\tau_{eff}}{\tau_{eff} + \tau_2} \cdot \frac{E_{ph}}{e}. \quad (2.25)$$

The slope efficiency S now reads

$$S = \eta_{extr} \eta_{int} = \frac{\alpha_m}{\alpha_m + \alpha_w} \cdot \eta_{inj} \cdot N \frac{\tau_{eff}}{\tau_{eff} + \tau_2} \cdot \frac{E_{ph}}{e}, \quad (2.26)$$

where η_{extr} is given in Eqn. (2.8).

We now have all the components for the WPE calculation. The output optical power P_{out} can be expressed as

$$P_{out} = S(I - I_{th}) = \frac{\alpha_m}{\alpha_m + \alpha_w} \cdot \eta_{inj} \cdot N \frac{\tau_{eff}}{\tau_{eff} + \tau_2} \cdot \frac{E_{ph}}{e} \cdot (I - I_{th}), \quad (2.27)$$

and finally the WPE reads

$$\text{WPE} = \frac{P_{out}}{P_{in}} = \frac{\frac{\alpha_m}{\alpha_m + \alpha_w} \eta_{inj} N \frac{\tau_{eff}}{\tau_{eff} + \tau_2} \frac{E_{ph}}{e} (I - I_{th})}{I \cdot [N(E_{ph} + E_{def})/e + I \cdot R_p]} \quad (2.28)$$

However, Eqn. (2.28) is a rather complicated expression for the WPE. With some rearrangement of the terms, the meaning of Eqn. (2.28) becomes more comprehensible:

$$\text{WPE} = \left[\frac{E_{ph}}{E_{ph} + E_{def} + e \cdot I \cdot R_p / N} \right] \cdot \left[\frac{I - I_{th}}{I} \right] \cdot \left[\eta_{inj} \cdot \frac{\tau_{eff}}{\tau_{eff} + \tau_2} \right] \cdot \left[\frac{\alpha_m}{\alpha_m + \alpha_w} \right], \quad (2.29)$$

where the expressions in the four square brackets are denoted from left to right as the voltage efficiency, the current efficiency, the internal efficiency, and the optical extraction efficiency. The underlying physical meanings of the above individual efficiencies are palpable. The voltage efficiency reflects the fact that not all the voltage drop across the device contributes to the radiative transitions, the energy defect between the lower laser state and the upper laser state in the next period as well as the parasitic voltage drop on the contacts and waveguide structures lowers the voltage efficiency. The current efficiency states that only the fraction of the current above the laser threshold contributes to the photon generation. The internal efficiency characterizes the probability for the occurrence of a photon emission when an electron transports through one stage of the active region/injector pair when the QC laser is operated above the threshold. The optical extraction efficiency, as explained previously, is the fraction of the generated photons that eventually escape the laser cavity and become utilizable optical power.

The WPE of QC lasers can be improved by improving any of the aforementioned efficiencies. The voltage efficiency can be improved by reducing the energy defect in the band-structure design [8], however, an insufficient energy defect would not effectively suppress the thermal backfilling effect at high operating temperatures and/or in CW operation, so the potential for improvement is rather limited. The optical collection efficiency can be improved by reducing the waveguide loss which also benefits the current efficiency, or increasing the mirror loss through tailoring the cavity length or applying anti-reflection coatings. However, increasing the mirror loss also degrades the threshold current density and the current efficiency, therefore, the mirror loss should be optimized in order to maximize the WPE [9].

The internal efficiency and the current efficiency are highly dependent on the band-structure determined parameters of the QC lasers. The internal efficiency can be increased by either optimizing the $\tau_{eff}/(\tau_{eff} + \tau_2)$ term or improving the electron injection efficiency η_{inj} , both of which are closely related to the band-structure and readily adjustable by design.

The term $\tau_{eff}/(\tau_{eff} + \tau_2)$ can be improved by increasing the relaxation lifetimes associated with the upper laser state ($\tau_{32}, \tau_{31}, \tau_3$) and/or reducing the relaxation lifetime associated with the lower laser state (τ_2). Making the radiative transition more diagonal decreases the spatial overlap of the upper laser state with the lower laser state and the other states below, therefore increases the corresponding relaxation lifetimes ($\tau_{32}, \tau_{31}, \tau_3$). Positioning at least one state at one LO-phonon energy (~ 34 meV) below the lower laser state helps to depopulate the lower laser state via LO-phonon scattering and reduces τ_2 . Meanwhile, both design strategies also benefit the population inversion and as a consequence may decrease the laser threshold current density; however, a more diagonal design may also significantly reduce the dipole moment for the radiative transition and consequently compromise the increased population inversion and reduce the optical gain, and therefore should be carefully employed when designing the band-structure of QC lasers.

On the other hand, one way to improve the electron injection efficiency η_{inj} is to speed up the electron injection process, i.e. the electron transport through the injector to the upper laser state in the downstream period. As the electron injection into the upper laser state becomes faster, the electron transport through leakage paths becomes less significant, and thus the injection efficiency η_{inj} is higher. Faster electron injection not only benefits the internal efficiency, but also improves the current efficiency from two aspects. First of all, a higher η_{inj} results in a better population inversion at any given current density and hence lowers the threshold current density. Secondly, a faster electron transport allows for a larger roll-over current density, i.e. the current density beyond which the output optical power begins to decrease as shown in Fig. 2.2. From the aforementioned steady state rate equations Eqns. (2.16)-(2.19) in combination with Eqns. (2.13)-(2.14), the current through the device structure is derived to be

$$I = \frac{N_1}{\tau_{inj}} = \frac{\tau_{31} + \tau_2}{2\tau_2\tau_{31} + \tau_2\tau_{inj} + \tau_{31}\tau_{inj}} N_{total} - \frac{\tau_{31} - \tau_2}{2\tau_2\tau_{31} + \tau_2\tau_{inj} + \tau_{31}\tau_{inj}} \cdot \frac{V_{ph}}{c \cdot \tau_{ph} \cdot \sigma \cdot \Gamma}$$

$$\approx \frac{1}{2\tau_2 + \tau_{inj}} N_{total} - \frac{1}{2\tau_2 + \tau_{inj}} \cdot \frac{V_{ph}}{c \cdot \tau_{ph} \cdot \sigma \cdot \Gamma} \quad (\text{since } \tau_{31} \gg \tau_2), \quad (2.30)$$

where τ_{inj} is sensitively dependent on the band-structure configuration strongly influenced by the applied external electric field. The maximum current through the structure is achieved when τ_{inj} assumes its minimum value under the specific bias condition. Although the peak WPE of a QC laser is usually reached somewhere before the roll-over current density, a larger roll-over current density in general dictates a higher current efficiency that can be achieved. Briefly stated, speeding up the electron transport from the injector ground state to the upper laser state is a key to the laser performance improvements, including lower threshold current density, higher slope efficiency and higher WPE.

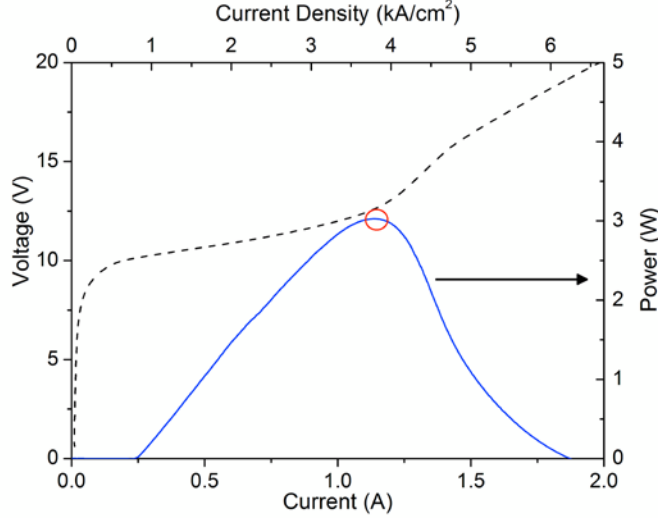


Fig. 2.2 Light-current-voltage (LIV) characteristics for a typical QC lasers. The roll-over current (density) is indicated by the red circle on the LI curve.

2.2 Electron transport in QC structures

As briefly discussed in Chapter 1, the electron transport from the lower laser state through the whole injector to the upper laser state in the next stage occurs mainly via a combination of phonon-assisted scattering [10], interface roughness induced scattering [10,11], and resonant tunneling [12].

Among all the phonon-assisted scattering processes, scattering assisted by the emission of LO-phonons which is present at any temperature is the dominant process [10] for intersubband transitions. Among the active region ground states and within the mini-band of the injector states, the LO-phonon-assisted scattering processes undergo multiple paths and are relatively fast with relaxation times on the order of 0.1 ps [10]; therefore they usually do not form the bottleneck for the electron transport.

The interface roughness refers to the random surface profile of the interface between the two adjacent layers of different materials. Such interface roughness can be seen clearly from the scanning tunneling microscope (STM) image of an InGaAs/AlInAs superlattice structure shown in Fig. 2.3. The profile of the interface roughness in the direction perpendicular to the material layers $h(\vec{r})$ is usually modeled as a random function with a Gaussian autocorrelation function [13]:

$$\int h(\vec{r})h(\vec{r} - \vec{r}_1)d\vec{r} = \Delta^2 e^{-|\vec{r}_1|^2/\Lambda^2}, \quad (2.31)$$

where \vec{r} and \vec{r}_1 are vectors within the nominal interface between the two layers, Δ is the mean square roughness height, and Λ is the correlation length. Although the device structures are

essentially grown atomic layer by atomic layer, the interface roughness cannot be eliminated with the current material growth technologies, and the associated parameters (Δ and Λ) are critically dependent on the growth conditions [14]. The interface roughness is essentially a perturbation to the bandstructure, and it introduces both intersubband scattering between different quantized subbands and intrasubband scattering within individual quantized subbands, and hence has critical influences on the device operation and performance. Similar to LO-phonon-assisted scattering, the intersubband scattering processes induced by interface roughness directly contribute to the electron transport. The interface roughness induced intersubband scattering is an elastic scattering process, and the scattering rate satisfies the expression [11]:

$$\hbar\tau_{21}^{-1} = \frac{\pi m^*}{\hbar^2} \Delta^2 \Lambda^2 \delta U^2 \sum_i \{\phi_1(z_i)\phi_2(z_i)\}^2 e^{-\Lambda^2 k_{21}^2/4}, \quad (2.32)$$

where m^* is the electron effective mass in the quantum well material, δU is the band offset associated with the two different materials composing the semiconductor heterostructure, ϕ_1 and ϕ_2 are the wavefunctions of the two concerned quantized states, respectively, z_i is the position of the i_{th} interface in the entire structure, and k_{21} is the momentum change associated with the intersubband scattering process as shown in Fig. 2.4. Such interface roughness induced intersubband scattering processes also take place between multiple pairs of subband states, and estimations of their scattering rates based on conventionally accepted values of the key material parameters (e.g., $\Delta \approx 0.15$ nm, $\Lambda \approx 6$ nm) have shown that interface roughness induced intersubband scattering rates are comparable to those associated with the LO-phonon assisted scattering [15]. Thus, interface roughness induced intersubband scattering also contributes significantly to the electron depopulation from the lower laser state within the active region as well as the electron transport within the injector.

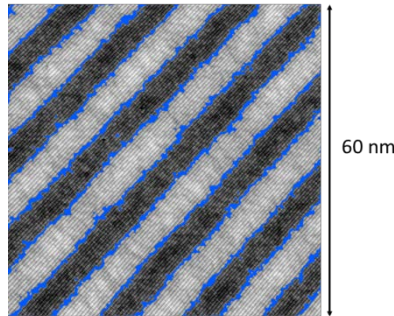


Fig. 2.3 STM image of a superlattice structure (InGaAs/AlInAs). The interface between neighboring material layers are highlighted in blue. (Courtesy of Mathew Woods, Federico Lopez, Kara Kanedy and Michael Weimer, Texas A&M University.)

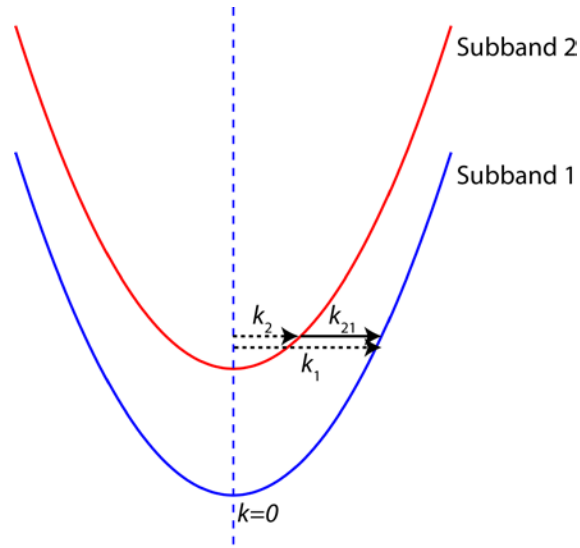


Fig. 2.4 Schematic of the interface-roughness-induced elastic intersubband scattering process.

Both the LO-phonon-assisted scattering and the interface-roughness-induced scattering require spatial overlap between the two subband wavefunctions. When the two concerned wavefunctions are relatively spatially separated, such scattering mechanisms are drastically suppressed, and the electron transport between the two subbands mainly relies on resonant tunneling when their energy levels are sufficiently close. In fact, for most conventional QC laser designs, the electron transport from the injector ground state to the upper laser state in the next stage occurs mainly via resonant tunneling because a thick injection barrier (also usually the thickest barrier in the entire structure) is usually employed which spatially separates the downstream active region from the injector. A major advantage of such a resonant tunneling based electron transport process is that it facilitates selective injection of electrons onto the upper laser state. In addition, the last barrier of the active region (exit barrier) is also usually designed to be relatively thick (one benefit for such a band-structure configuration is to have the ground states in the active region sufficiently confined so that electrons can quickly depopulate from the lower laser state to the states below via scattering processes), that electrons transport from the ground state in the active region to the injector states also via resonant tunneling. Theoretical study on the resonant tunneling of electrons through thick potential barriers suggests that the tunneling rate can be severely suppressed by various mechanisms and consequently become the bottleneck of the electron transport process. On the other hand, the electron transport among injector states may occasionally also rely on resonant tunneling processes, however, since the barriers in the injector are usually much thinner in comparison, such resonant tunneling processes within the injector are less likely to be bottlenecks. Nevertheless, several design strategies have been demonstrated to reduce the electron transport time within the injector, such as the short injector designs [16] and the injectorless designs [17,18], however, they did not focus on optimizing the resonant tunneling process through the thick injection barrier.

The resonant tunneling process is a coherent process, meaning that the phase information of the concerned states influences the transitions and is preserved during the transitions, therefore it should not be treated as a scattering process with an effective lifetime which can be incorporated in rate equations similar to those in the previous section (the phase information is irrelevant in such scattering processes). Instead, such a coherent process can be readily described and studied within the density matrix formalism [19-23]. To study the resonant tunneling process in QC lasers, we can simplify the entire band-structure as a periodic two-level system as shown in Fig. 2.5. Since the most crucial resonant tunneling process in the QC laser operation is the one between the injector ground state and the downstream upper laser state through the thick injection barrier, the simple model illustrated in Fig. 2.5 can be considered as an abstract picture for this critical process with state 1 representing the injector ground state and the state 2 representing the downstream upper laser state.

In this periodic band-structure, the thick injection barriers are treated as the boundaries between individual periods, therefore, states 1 and 2 are not eigenstates of the entire periodic structure, but instead are the localized eigenstates belonging to two different periods, respectively. In reality, when state 1 and state 2 are energetically close to each other under a certain bias electric field range, they will couple together and form a pair of eigenstates associated with the entire periodic structure that extend across both periods, similar to two atoms forming bonds. Such “true” eigenstates of the entire periodic structure can be constructed as the linear combination of state 1 and state 2 with the tight binding formalism. These true eigenstates have an energy separation between themselves that changes monotonously with the absolute value of the energy detuning between state 1 and state 2 ($\Delta_{1,2}$). The energy separation reaches its minimum value $2|\Omega_{1,2}|$ when $\Delta_{1,2}=0$, where $\Omega_{1,2}$ is defined as the coupling strength between state 1 and state 2 when they are energetically in resonance and is given by

$$\Omega_{1,2} = \langle \phi_1 | \hat{H} | \phi_2 \rangle = \int_{-\infty}^{\infty} \phi_1^* \hat{H} \phi_2 dz = \Omega_{2,1}^* , \quad (2.33)$$

Where ϕ_1 and ϕ_2 are the wavefunctions for state 1 and state 2, respectively, and \hat{H} is the Hamiltonian associated with the entire periodic structure.

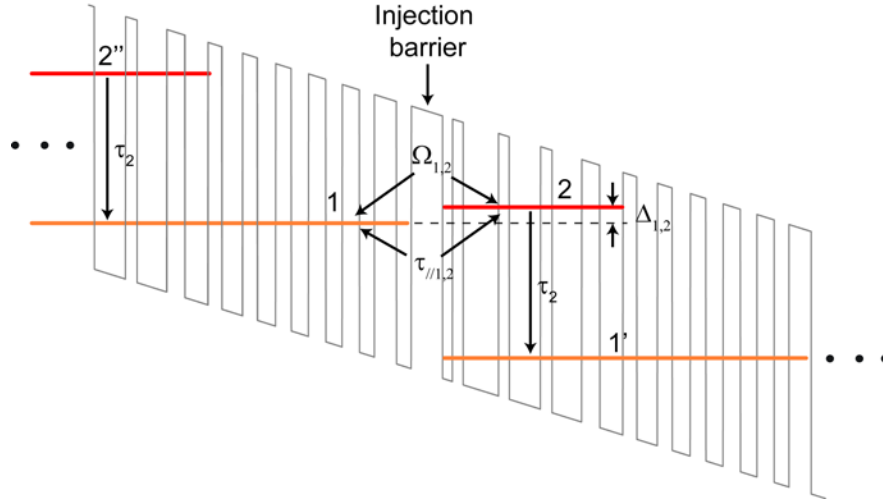


Fig. 2.5 Schematic of the periodic two-level system model for studying the resonant tunneling process through the thick injection barrier in QC lasers.

In order to study the resonant tunneling process between the injector ground state and the downstream upper laser state in QC lasers based on the simplified system model in Fig. 2.5, we further assume the phenomenological population relaxation time for the upper laser state is τ_2 , and the corresponding relaxed electron population all transitions to the injector ground state below. Such a phenomenological relaxation process takes into account various intersubband scattering processes as well as the stimulated emission when operated above the threshold, while the model remains considerably simple. Furthermore, the dephasing time associated with this coherent process is designated $\tau_{||1,2}$.

The state of the system is described by the following density matrix

$$\hat{\rho} = \begin{bmatrix} \rho_{11} & \rho_{12} \\ \rho_{21} & \rho_{22} \end{bmatrix}, \quad (2.34)$$

where ρ_{11} and ρ_{22} are the probability that the system is in state 1 and state 2, respectively, and $\rho_{12} = \rho_{21}^*$ characterizes the coherence between state 1 and state 2. The time evolution of the above density matrix is given by

$$\frac{d\hat{\rho}}{dt} = \frac{-i}{\hbar} [\hat{H}, \hat{\rho}] - \begin{bmatrix} \frac{-\rho_{22}}{\tau_2} & \frac{\rho_{12}}{\tau_{||1,2}} \\ \frac{\rho_{21}}{\tau_{||1,2}} & \frac{\rho_{22}}{\tau_2} \end{bmatrix} = \frac{-i}{\hbar} [\hat{H}\hat{\rho} - \hat{\rho}\hat{H}] - \begin{bmatrix} \frac{-\rho_{22}}{\tau_2} & \frac{\rho_{12}}{\tau_{||1,2}} \\ \frac{\rho_{21}}{\tau_{||1,2}} & \frac{\rho_{22}}{\tau_2} \end{bmatrix}, \quad (2.35)$$

where \hat{H} written in the matrix form is

$$\hat{H} = \begin{bmatrix} E_1 & \Omega_{1,2} \\ \Omega_{2,1} & E_1 + \Delta_{1,2} \end{bmatrix}, \quad (2.36)$$

where E_1 is the energy for state 1.

Since we are mostly interested in the steady state solutions for the above density matrix equations, therefore setting Eqn. (2.35) equal to zero and expanding it with Eqn. (2.36), the following independent equations for the density matrix elements are obtained:

$$\frac{i}{\hbar} (\rho_{12}\Omega_{2,1} - \rho_{21}\Omega_{1,2}) + \frac{\rho_{22}}{\tau_2} = 0, \quad (2.37)$$

$$\frac{i}{\hbar} (\rho_{11} - \rho_{22})\Omega_{1,2} + \frac{i}{\hbar} \rho_{12}\Delta_{1,2} - \frac{\rho_{12}}{\tau_{\parallel 1,2}} = 0. \quad (2.38)$$

Because the system is closed, the total population is conserved, therefore we also have

$$\rho_{11} + \rho_{22} = 1. \quad (2.39)$$

From Eqns. (2.37)-(2.39), the steady state solutions for ρ_{11} and ρ_{22} are found to be

$$\rho_{11} = \frac{1 + \Delta_{1,2}^2 \tau_{\parallel 1,2}^2 / \hbar^2 + 2|\Omega_{1,2}|^2 \tau_{\parallel 1,2} \tau_2 / \hbar^2}{1 + \Delta_{1,2}^2 \tau_{\parallel 1,2}^2 / \hbar^2 + 4|\Omega_{1,2}|^2 \tau_{\parallel 1,2} \tau_2 / \hbar^2}, \quad (2.40)$$

$$\rho_{22} = \frac{2|\Omega_{1,2}|^2 \tau_{\parallel 1,2} \tau_2 / \hbar^2}{1 + \Delta_{1,2}^2 \tau_{\parallel 1,2}^2 / \hbar^2 + 4|\Omega_{1,2}|^2 \tau_{\parallel 1,2} \tau_2 / \hbar^2}. \quad (2.41)$$

In steady state, the rate of electrons moving from state 1 to state 2 via resonant tunneling should match the rate of electrons scattered out of state 2 due to the continuity of the current density, therefore the resonant tunneling current density through the structure is given by

$$J_{RT} = \frac{\tilde{N}_2}{\tau_2} = \frac{\rho_{22} \tilde{N}_{total}}{\tau_2} = \tilde{N}_{total} \cdot \frac{2|\Omega_{1,2}|^2 \tau_{\parallel 1,2} / \hbar^2}{1 + \Delta_{1,2}^2 \tau_{\parallel 1,2}^2 / \hbar^2 + 4|\Omega_{1,2}|^2 \tau_{\parallel 1,2} \tau_2 / \hbar^2}. \quad (2.42)$$

where \tilde{N}_2 is the sheet electron density on state 2, and \tilde{N}_{total} is the total sheet electron density per period of active region/injector pair and is determined by the doping density.

2.3 Role of interface roughness in key resonant tunneling processes

According to Eqn. (2.42), the resonant tunneling current density is critically dependent on the dephasing time $\tau_{\parallel 1,2}$. For mid-IR QC lasers, the dominant dephasing mechanism (in-plane

momentum relaxation) associated with the intersubband transitions is the interface roughness induced intrasubband scattering [11,24,25], while the dephasing also has contributions from all the other scattering processes including LO-phonon scattering, interface roughness induced intersubband scattering, impurity scattering, electron-electron scattering, etc. Such dephasing mechanisms cause linewidth broadening of the associated transitions. Neglecting all the other contributions, the intersubband transition (state 1 \rightarrow state 2) linewidth broadening associated with the interface roughness induced intrasubband scattering is given by [20,25]

$$\hbar\tau_{\parallel 1,2}^{-1} = \frac{\pi m^*}{\hbar^2} \Delta^2 \Lambda^2 \delta U^2 \sum_i \{ \phi_1^2(z_i) - \phi_2^2(z_i) \}^2, \quad (2.43)$$

where all the parameters are defined as in the previous section. Apparently, the linewidth broadening of different transitions are all different due to the factor $\sum_i \{ \phi_1^2(z_i) - \phi_2^2(z_i) \}^2$, which can be readily calculated from the band-structure. The linewidth broadening (or equivalently the dephasing time) associated with the resonant tunneling process is difficult to be directly measured, and its estimation requires knowledge on the material parameters including Δ and Λ where are also quite challenging to characterize [26]. Fortunately, the spectra of the spontaneous emission of QC lasers which corresponds to the intersubband transition between the upper laser state and the lower laser state can be easily measured, and the factor $\frac{\pi m^*}{\hbar^2} \Delta^2 \Lambda^2 \delta U^2$ can be extracted from its linewidth and the calculation of its wavefunction factor. With such a result, the linewidth of all the other intersubband transitions can be estimated.

When carrying out such linewidth estimation, one usually finds that the broadening associated with the resonant tunneling between the injector ground state and the downstream upper laser state is much larger than that of the spontaneous emission. This is mainly due to the difference in the $\sum_i \{ \phi_1^2(z_i) - \phi_2^2(z_i) \}^2$ factors: for the spontaneous emission, the upper laser state and the lower laser state have significant spatial overlap at the interfaces within the active region, therefore $\phi_1^2(z_i)$ and $\phi_2^2(z_i)$ cancel each other and $\{ \phi_1^2(z_i) - \phi_2^2(z_i) \}^2$ is relatively small; on the other hand, for the resonant tunneling process, the injector ground state and the downstream upper laser state have little spatial overlap at the interfaces where either wavefunction is present, therefore $\{ \phi_1^2(z_i) - \phi_2^2(z_i) \}^2$ is relative large. Such an observation can also be understood intuitively from the following picture. The interface roughness induced broadening to the intersubband transitions originates from the shifting of the energy levels of the states involved as a result of the fluctuations of the quantum wells' thicknesses introduced by the interface roughness. Therefore, if the two states are spatially located in the same region, then the fluctuation of the quantum wells' thicknesses shift their energy levels in the same direction, and the transition energy changes significantly less; however, if the two states are spatially located in different regions, then the fluctuation of the quantum wells' thicknesses shift their energy levels in uncorrelated directions, and the transition energy changes significantly more, leading to much larger broadening.

2.4 Optimization of the coupling strength

The broadening associated with the resonant tunneling between the injector ground state and the downstream upper laser state is usually a few times larger than that of the spontaneous emission. For QC lasers operating around the 4 μm to 5 μm range, the full width at half maximum (FWHM) of the spontaneous emission spectrum is typically ~ 25 meV, which suggests the broadening of the resonant tunneling process is on the order of 100 meV, corresponding to a dephasing time of a few femtoseconds (~ 5 fs would be a reasonable estimation for $\tau_{\parallel 1,2}$). For such short dephasing time which is mostly determined by the material growth technology and therefore difficult to change, the resonant tunneling current density described by Eqn. (2.42) can be severely limited. However, it is possible to overcome such negative effect of the fast dephasing process from the band-structure design perspective. An effective way is to increase the coupling strength between the injector ground state and the downstream upper laser state since J_{RT} increases monotonously with $|\Omega_{1,2}|^2$. Without loss of generality, we can focus on the resonant tunneling current density when the two states are in full resonance, i.e. $\Delta_{1,2} = 0$, and Eqn. (2.42) becomes

$$J_{RT,max} = \tilde{N}_{total} \cdot \frac{2|\Omega_{1,2}|^2 \tau_{\parallel 1,2} / \hbar^2}{1 + 4|\Omega_{1,2}|^2 \tau_{\parallel 1,2} \tau_2 / \hbar^2} \quad (2.44)$$

where $J_{RT,max}$ is the maximum current density that can be supported by this resonant tunneling process. According to Eqn. (2.44) $J_{RT,max}$ increases when the coupling strength $|\Omega_{1,2}|$ becomes larger, but eventually when $4|\Omega_{1,2}|^2 \tau_{\parallel 1,2} \tau_2 \gg \hbar^2$, $J_{RT,max}$ saturates at $\frac{\tilde{N}_{total}}{2\tau_2}$ which is no longer limited by the resonant tunneling process but by the upper laser state lifetime, and this is referred to as the strong coupling regime [12]. Further increase of $|\Omega_{1,2}|$ no longer benefits the resonant tunneling current density, however, it increases the energy splitting (equals $2|\Omega_{1,2}|$) between the pair of extended eigenstates formed by the localized in-resonance states. In the picture of extended eigenstates, both eigenstates contribute to the optical gain, therefore a larger energy splitting between them leads to a broader optical gain spectrum and a lower peak gain coefficient, which is harmful for the laser threshold performance. These facts suggest there is a trade-off between the resonant tunneling current density and the gain profile, and the coupling strength within an optimal range should be employed to optimize the laser overall performance.

In most conventional designs, the employed coupling strength between the injector ground state and the downstream upper laser state was in the range from 2 meV to 4 meV, and such a coupling strength was prevalently believed to be just entering the strong coupling regime and thus the resonant tunneling current density was optimized. On the other hand, since the energy splitting between the anti-crossed states is significantly smaller than the broadening of the energy level of individual states, quite conveniently, the optical gain profile is also well maintained in this way. This seems to be a satisfying solution to the task of coupling strength optimization. However, an oversimplified assumption made to estimate the commencement of

the strong coupling regime was long neglected: the dephasing time (or equivalently the transition linewidth broadening) associated with the resonant tunneling process was assumed to be identical to that of the spontaneous emission. For example, the optical gain spectrum width for QC lasers operating around 4 μm to 5 μm range is around 25 meV, corresponding to a dephasing time of ~ 25 fs. The typical value for the upper laser state lifetime is ~ 5 ps. Therefore, in order to achieve the strong coupling regime $4|\Omega_{1,2}|^2 \tau_{\parallel 1,2} \tau_2 \gg \hbar^2$ dictates that $|\Omega_{1,2}| \gg 1$ meV, and $|\Omega_{1,2}| \sim 3$ meV would be sufficient for the QC laser to operate in the strong coupling regime. However, from Eqn. (2.43) we know that the dephasing time associated with the resonant tunneling process is actually much smaller, therefore the coupling strength employed in most conventional designs is not sufficient to overcome such fast dephasing process and reach the strong coupling regime. Intuitively, the straightforward solution is to further increase the coupling strength. If the dephasing time of the resonant tunneling process is a quarter of that of the spontaneous emission, then the coupling strength should approximately be doubled.

Nevertheless, a more comprehensive density matrix based model was developed to investigate this issue and pinpoint the optimal range for the coupling strength [20]. This model is based on a periodic three-level system which includes the injector state (1), the upper laser state (3) and the lower laser state (2) in one QC laser stage confined by the injection barriers as shown in Fig. 2.6. The model presented below is similar to that in [20] and it takes into account the dephasing times for the transitions between each pair of states ($\tau_{\parallel 1,2}$, $\tau_{\parallel 1,3}$, and $\tau_{\parallel 2,3}$ respectively) and the scattering relaxation time between state 3 and state 2 (τ_3) as well as that between state 2 and state 1 (τ_2), however, the thermal backfilling term is not included. Defining the upper laser state 3 to be at the zero energy level, the time evolution equations of the density matrix is given by

$$\frac{d}{dt} \begin{pmatrix} \rho_{11} & \rho_{12} & \rho_{13} \\ \rho_{21} & \rho_{22} & \rho_{23} \\ \rho_{31} & \rho_{32} & \rho_{33} \end{pmatrix} = \frac{i}{\hbar} \left[\begin{pmatrix} \rho_{11} & \rho_{12} & \rho_{13} \\ \rho_{21} & \rho_{22} & \rho_{23} \\ \rho_{31} & \rho_{32} & \rho_{33} \end{pmatrix}, \begin{pmatrix} -\delta_{1,3} & 0 & \Omega_{1,3} \\ 0 & -(\hbar\omega + \Delta_{3,2}) & \Omega_l \exp(i\omega t) \\ \Omega_{3,1} & \Omega_l \exp(-i\omega t) & 0 \end{pmatrix} \right] - \begin{pmatrix} -\rho_{22}\tau_2^{-1} & \rho_{12}\tau_{\parallel 1,2}^{-1} & \rho_{13}\tau_{\parallel 1,3}^{-1} \\ \rho_{21}\tau_{\parallel 1,2}^{-1} & \rho_{22}\tau_2^{-1} - \rho_{33}\tau_3^{-1} & \rho_{23}\tau_{\parallel 2,3}^{-1} \\ \rho_{31}\tau_{\parallel 1,3}^{-1} & \rho_{32}\tau_{\parallel 2,3}^{-1} & \rho_{33}\tau_3^{-1} \end{pmatrix}, \quad (2.45)$$

where Ω_l is the Rabi frequency associated with the optical field and is defined as (in the unit of energy)

$$\Omega_l = 2e|z_{32}| \cdot |E|, \quad (2.46)$$

where E is the electric component of the optical field, and z_{32} is the dipole moment associated with the intersubband transition from state 3 to state 2 and is given by

$$z_{32} = \int_{-\infty}^{\infty} \phi_3^* z \phi_2 dz. \quad (2.47)$$

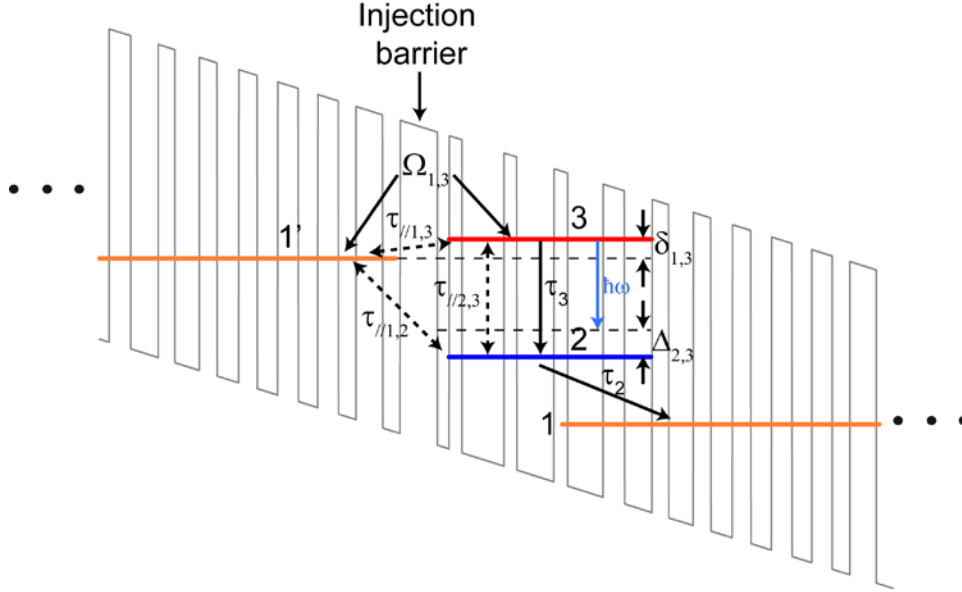


Fig. 2.6 Schematic of the density matrix model based on a periodic three-level system.

Again, we have conservation of the total electron population on the three subbands

$$\rho_{11} + \rho_{22} + \rho_{33} = 1. \quad (2.48)$$

From Eqn. (2.45) we see that the coherence terms $\rho_{32}, \rho_{23}, \rho_{21}, \rho_{12}$ is driven by the fast changing optical field $\Omega_l \exp(-i\omega t)$ or $\Omega_l \exp(i\omega t)$, therefore when the photon energy $\hbar\omega$ is close to the transition energy between state 3 and state 2, and the detuning $\delta_{1,3}$ between state 1' and state 3 is small, we expect the coherence terms $\rho_{32}, \rho_{23}, \rho_{21}, \rho_{12}$ to oscillate in the same frequency ω as the optical field, and the corresponding solutions of Eqn. (2.45) should have the form:

$$\rho_{23} = \bar{\rho}_{23} \exp(i\omega t), \quad (2.49a)$$

$$\rho_{32} = \bar{\rho}_{32} \exp(-i\omega t), \quad (2.49b)$$

$$\rho_{21} = \bar{\rho}_{21} \exp(i\omega t), \quad (2.49c)$$

$$\rho_{12} = \bar{\rho}_{12} \exp(-i\omega t), \quad (2.49d)$$

where $\bar{\rho}_{23}, \bar{\rho}_{32}, \bar{\rho}_{21}, \bar{\rho}_{12}$ have much slower time evolution than $\exp(\mp i\omega t)$. If we substitute Eqn. (2.49) into Eqn. (2.45), then after rearrangement it becomes

$$\frac{d}{dt} \begin{pmatrix} \rho_{11} & \bar{\rho}_{12} & \rho_{13} \\ \bar{\rho}_{21} & \rho_{22} & \bar{\rho}_{23} \\ \rho_{31} & \bar{\rho}_{32} & \rho_{33} \end{pmatrix} = \frac{i}{\hbar} \left[\begin{pmatrix} \rho_{11} & \bar{\rho}_{12} & \rho_{13} \\ \bar{\rho}_{21} & \rho_{22} & \bar{\rho}_{23} \\ \rho_{31} & \bar{\rho}_{32} & \rho_{33} \end{pmatrix}, \begin{pmatrix} -\delta_{1,3} & 0 & \Omega_{1,3} \\ 0 & -(\hbar\omega + \Delta_{3,2}) & \Omega_l \exp(i\omega t) \\ \Omega_{3,1} & \Omega_l \exp(-i\omega t) & 0 \end{pmatrix} \right] - \begin{pmatrix} -\rho_{22}\tau_2^{-1} & \bar{\rho}_{12}\tau_{\parallel 1,2}^{-1} & \rho_{13}\tau_{\parallel 1,3}^{-1} \\ \bar{\rho}_{21}\tau_{\parallel 1,2}^{-1} & \rho_{22}\tau_2^{-1} - \rho_{33}\tau_3^{-1} & \bar{\rho}_{23}\tau_{\parallel 2,3}^{-1} \\ \rho_{31}\tau_{\parallel 1,3}^{-1} & \bar{\rho}_{32}\tau_{\parallel 2,3}^{-1} & \rho_{33}\tau_3^{-1} \end{pmatrix}. \quad (2.50)$$

In general the coupling strength $\Omega_{1,3}$ is complex, here for simplicity we assume $\Omega_{1,3}$ is real and therefore $\Omega_{1,3} = \Omega_{3,1} = \Omega_c$. The off-diagonal density matrix elements are also complex and satisfy $\bar{\rho}_{ij} = \rho_{ji}^*$, where $i, j \in [1,2,3]$ and $i \neq j$. Therefore, the independent variables in Eqn. (2.50) can be chosen as the following 9 variables in total:

ρ_{11} , $\text{Re}(\bar{\rho}_{12})$, $\text{Im}(\bar{\rho}_{12})$, $\text{Re}(\rho_{13})$, $\text{Im}(\rho_{13})$, ρ_{22} , $\text{Re}(\bar{\rho}_{23})$, $\text{Im}(\bar{\rho}_{23})$, and ρ_{33} , where $\text{Re}(x)$ and $\text{Im}(x)$ represent the real and the imaginary parts of x , respectively.

In order to find the steady state solutions for the 9 independent density matrix variables, we can set the left side of Eqn. (2.50) to be 0 and solve it in combination with Eqn. (2.48). In the steady state condition Eqn. (2.50) and Eqn. (2.48) can be expanded to form a set of 9 independent linear equations which are shown below:

$$\begin{bmatrix} 0 & 0 & 0 & 0 & -2\Omega_c & \hbar\tau_2^{-1} & 0 & 0 & 0 \\ 0 & \hbar\tau_{\parallel 1,2}^{-1} & -(\Delta_{2,3} - \delta_{1,3}) & 0 & \Omega_l & 0 & 0 & \Omega_c & 0 \\ 0 & (\Delta_{2,3} - \delta_{1,3}) & \hbar\tau_{\parallel 1,2}^{-1} & -\Omega_l & 0 & 0 & \Omega_c & 0 & 0 \\ 0 & 0 & \Omega_l & \hbar\tau_{\parallel 1,3}^{-1} & \delta_{1,3} & 0 & 0 & 0 & 0 \\ \Omega_c & \Omega_l & 0 & \delta_{1,3} & -\hbar\tau_{\parallel 1,3}^{-1} & 0 & 0 & 0 & -\Omega_c \\ 0 & 0 & 0 & 0 & 0 & \hbar\tau_2^{-1} & 0 & 2\Omega_l & -\hbar\tau_3^{-1} \\ 0 & \Omega_c & 0 & 0 & 0 & \Omega_l & \Delta_{2,3} & -\hbar\tau_{\parallel 2,3}^{-1} & -\Omega_l \\ 0 & 0 & \Omega_c & 0 & 0 & 0 & -\hbar\tau_{\parallel 2,3}^{-1} & -\Delta_{2,3} & 0 \\ 1 & 0 & 0 & 0 & 0 & 1 & 0 & 0 & 1 \end{bmatrix} \times \begin{pmatrix} \rho_{11} \\ \text{Re}(\bar{\rho}_{12}) \\ \text{Im}(\bar{\rho}_{12}) \\ \text{Re}(\rho_{13}) \\ \text{Im}(\rho_{13}) \\ \rho_{22} \\ \text{Re}(\bar{\rho}_{23}) \\ \text{Im}(\bar{\rho}_{23}) \\ \rho_{33} \end{pmatrix} = \begin{pmatrix} 0 \\ 0 \\ 0 \\ 0 \\ 0 \\ 0 \\ 0 \\ 0 \\ 1 \end{pmatrix}. \quad (2.51)$$

One of the most interesting parameters that can be extracted from Eqn. (2.51) for the steady state density matrix elements is the optical gain $g(\omega)$, given by the expression [23]

$$g(\omega) = \frac{\tilde{N}_s e^2 n_{eff} |z_{32}|^2 \omega}{2d\epsilon_0 \epsilon_r c \Omega_l} \text{Im}(\bar{\rho}_{23}), \quad (2.52)$$

where \tilde{N}_s is the sheet doping density per period of active region/injector pair whose thickness is d , n_{eff} is the effective modal refractive index of the waveguide, $\epsilon_0 \epsilon_r$ is the permittivity of the material, and c is the speed of light in vacuum. From Eqn. (2.51)-(2.52), the optical gain is solved to be

$$\begin{aligned}
g(\omega) &= \frac{2\tilde{N}_s e^2 n_{eff} |z_{32}|^2 \omega}{d\epsilon_0 \epsilon_r c \Omega_l} \text{Im}(\bar{\rho}_{23}) \approx \frac{4\tilde{N}_s e^2 n_{eff} |z_{32}|^2 \omega}{d\epsilon_0 \epsilon_r c} \times \frac{\Omega_c^2 \tau_{\parallel 1,2} \tau_{\parallel 2,3} (\tau_3 - \tau_2) / \hbar^2}{1 + \delta_{1,3}^2 \tau_{\parallel 1,3}^2 / \hbar^2 + 2\Omega_c^2 \tau_{\parallel 1,3} (2\tau_3 + \tau_2) / \hbar^2} \\
&\times \frac{1 + (\Delta_{2,3} - \delta_{1,3})^2 \tau_{\parallel 1,2}^2 / \hbar^2 + \Omega_c^2 \tau_{\parallel 1,2} \tau_{\parallel 2,3} / \hbar^2}{1 + (\Delta_{2,3} - \delta_{1,3})^2 \tau_{\parallel 1,2}^2 / \hbar^2 + 2\Omega_c^2 \tau_{\parallel 1,2} \tau_{\parallel 2,3} / \hbar^2 + (\Delta_{2,3}^2 / \hbar^2 + (\Omega_c^2 - \Delta_{2,3}^2 + \Delta_{2,3} \delta_{1,3})^2 \tau_{\parallel 1,2}^2 / \hbar^4) \tau_{\parallel 2,3}^2}. \quad (2.53)
\end{aligned}$$

We can further set the detuning terms $\Delta_{2,3}$ and $\delta_{1,3}$ to be 0 and obtain the peak optical gain as a function of the coupling strength Ω_c

$$g_{max} = \xi \times \frac{\Omega_c^2 \tau_{\parallel 1,2} \tau_{\parallel 2,3} (\tau_3 - \tau_2) / \hbar^2}{1 + 2\Omega_c^2 \tau_{\parallel 1,3} (2\tau_3 + \tau_2) / \hbar^2} \times \frac{1}{1 + \Omega_c^2 \tau_{\parallel 1,2} \tau_{\parallel 2,3} / \hbar^2}, \quad (2.54)$$

where

$$\xi = \frac{4\tilde{N}_s e^2 n_{eff} |z_{32}|^2 E_{32}}{\hbar d\epsilon_0 \epsilon_r c}, \quad (2.55)$$

and E_{32} is the laser transition energy. Figure 2.7 plots the g_{max}/ξ as a function of the coupling strength Ω_c , assuming $\tau_3 = 2$ ps, $\tau_2 = 0.2$ ps, and $\tau_{\parallel 2,3} = 66$ fs, $\tau_{\parallel 1,2} = 20$ fs, $\tau_{\parallel 1,3} = 13$ fs (corresponding to transition broadening of 20 meV, 66 meV and 100 meV, similar to those in [20]).

As we can see from Fig. 2.7, the peak optical gain increases monotonously with Ω_c at the beginning, and then saturates and roll-over at $\Omega_c \sim 10$ meV. For the typical value of $\Omega_c \sim 3$ meV employed in most convention QC laser designs, the peak optical gain is actually much lower than the maximum that is achievable. Therefore, in order to effectively suppress the interface roughness induced dephasing to the resonant tunneling process and optimize the optical gain, a much larger coupling strength Ω_c between the injector ground state and the upper laser state needs to be employed in the band-structure design. To distinguish it from the conventional strong coupling regime, we refer to this new design strategy as the ultra-strong coupling regime.

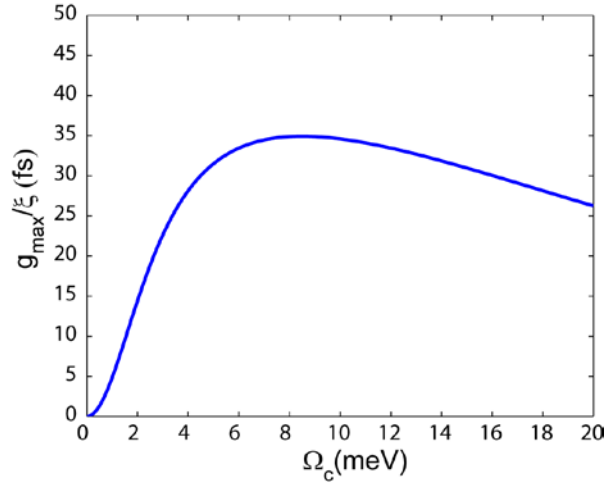


Fig. 2.7 The trend of the peak optical gain as a function of the coupling strength Ω_c .

2.5 High performance QC lasers employing ultra-strong coupling design strategy

Following the theoretical analysis of the optimal coupling strength between the injector ground state and the upper laser state, we incorporate the proposed ultra-strong coupling design strategy in real QC laser designs operating in the 4 μm to 5 μm range. In this section, we present one of the best performing designs with which a record WPE of QC lasers is achieved.

2.5.1 Band-structure design

In order to increase the coupling strength between the injector ground state and the downstream upper laser state, the spatial overlap between the decaying tails of the two wavefunctions needs to be enhanced, which can be perceived from Eqn. (2.33). A straightforward and effective way to achieve this goal is to decrease the thickness of the thick injection barrier between the two states. We employ such an approach in our ultra-strong coupling QC laser band-structure designs: by reducing the thickness of the injection barrier from a typical value of ~ 4 nm down to ~ 1 nm, the coupling strength can be significantly increased to ~ 10 meV, the estimated optimal range in the ultrastrong coupling regime. The band-structure for one of the best performing designs (wafer No. A785) is shown in Fig. 2.8 [27].

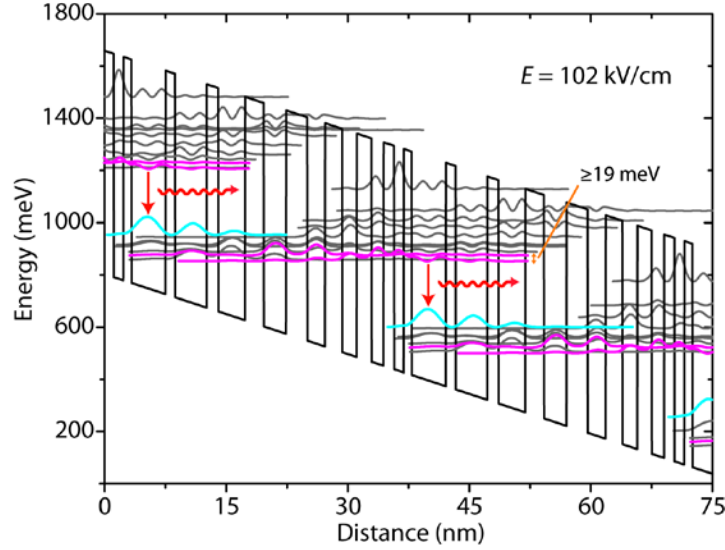


Fig. 2.8 Band-structure of one of the best performing ultra-strong coupling QC laser designs (wafer No. A785). Starting from the widest quantum well, the layer sequence of one period of the active region/injector pair in the electron downstream direction with individual thickness in nanometer is:

4.2/**1.2**/3.9/**1.4**/3.3/**2.3**/2.8/**2.6**/2.2/2.1/1.8/**1.8**/1.5/**1.3**/1.2/**1.0**, where the InAlAs barrier layers are in bold, the InGaAs well layers are in roman. The underlined layers are doped with a bulk doping density of $2.3 \times 10^{17} \text{ cm}^{-3}$, corresponding to a sheet doping density of $1 \times 10^{11} \text{ cm}^{-2}$ per period.

The above QC laser design employs an estimated optimal coupling strength Ω_c of ~ 10 meV (the energy splitting between the two anti-crossed red states in Fig. 2.8 is ~ 19 meV, corresponding to $2\Omega_c$), which is much stronger compared to those in conventional designs (~ 2 – 4 meV). This is achieved by adopting a much thinner injection barrier (~ 1 nm vs. ~ 3 – 4 nm in most conventional designs) between the injector and the active region. In addition, such a design approach has other benefits for the electron transport: the stronger coupling (thinner barrier) leads to stronger anti-crossing and a reduced Stark shift (i.e., the energy detuning due to the change in the applied electric field) between the injector ground state and the downstream upper laser state, which consequently make the alignment of the two energy levels more stable when subjected to a change in the external bias; and furthermore, the resonant tunneling rate also becomes less susceptible to the detuning between the two states according to Eqn. (2.42).

The wavefunctions plotted in Fig. 2.8 are the eigenstates of the entire periodic structure, therefore it can be difficult to extract the exact coupling strength between the injector ground state and the downstream upper laser state in such a picture due to the coupling with the other states. On the other hand, the whole structure can be divided at certain relatively thick barriers to form bases as shown in Fig. 2.9, and all the states including the injector ground state and the upper laser state are treated as eigenstates associated with the bases in which they are localized. In such a picture, the coupling strength between two states from different bases can be readily calculated with a tight-binding approach. With the choice of bases shown in Fig. 2.9, the coupling strength between the injector ground state (green) and the downstream upper laser state

(red) is calculated to be ~ 8.5 meV. However, it is worth noting that for this band-structure design the choice of bases are not absolutely decisive since no exceedingly thick barrier is present. The coupling strength calculation is critically dependent on the choice of bases and therefore contains a certain degree of ambiguity, nevertheless, it is clear that the coupling strength is significantly enhanced in this design in comparison with conventional designs.

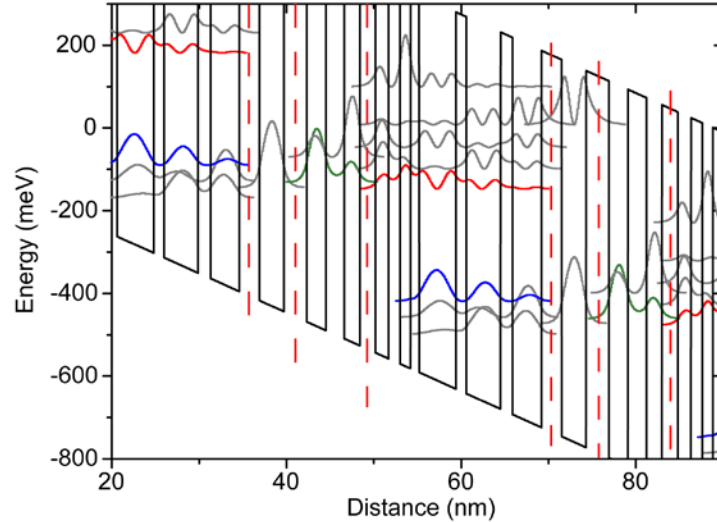


Fig. 2.9 Band-structure of the same design in Fig. 2.8 with the localized wavefunctions in the divided bases plotted. One period of active region/injector pair is divided into 3 bases at the barriers indicated by the red dashed lines.

Besides that the ultra-strong coupling is expected to effectively overcome the interface-roughness-induced dephasing of the resonant tunneling process and lead to a more optimal tunneling current, another concurrent advantage of such an ultra-strong coupling design is that the upper laser state spreads more into the injector region as a result of the thin injection barrier, so that the radiative transition is more diagonal rather than vertical, which increases the upper laser level lifetime and consequently improves the slope efficiency (see Eqn. (2.26)) and decreases the threshold current density thanks to a larger population inversion.

The entire band-structure design makes use of strain balanced InGaAs/AlInAs material system to provide large enough band-offset for the relatively short wavelength operation. The designed materials compositions are $\text{In}_{0.66}\text{Ga}_{0.34}\text{As}/\text{Al}_{0.69}\text{In}_{0.31}\text{As}$, and the corresponding band-offset is ~ 890 meV. The active region design is based on three quantum wells, the radiative transition energy is designed to be ~ 260 meV, and two resonant LO-phonons depopulation scheme [28] is adopted to efficiently depopulate the lower laser state (the blue state in Fig. 2.8). The injector consists of 5 quantum wells, within which a narrow and relatively flat miniband of several strongly coupled states are formed to facilitate the electron transport via a combination of different scattering mechanisms and resonant tunneling. The total energy defect for suppressing the thermal back-filling at high temperature is designed to be ~ 80 meV.

2.5.2 Waveguide structure design

The active core of this QC laser design contains 43 periods of active region/injector pairs with a total thickness of $\sim 1.5 \mu\text{m}$. In order to achieve a large mode confinement factor and a low waveguide loss, the following waveguide structure design is employed: from the substrate up, the layers sequence is (1) a $2 \mu\text{m}$ thick InP bottom waveguide cladding layer with low doping density of $2.0 \times 10^{16} \text{ cm}^{-3}$; (2) the $1.5 \mu\text{m}$ thick active core with average doping density of $2.9 \times 10^{16} \text{ cm}^{-3}$; (3) a $2.3 \mu\text{m}$ thick InP top waveguide cladding layer with low doping density of $2 \times 10^{16} \text{ cm}^{-3}$; (4) an additional $0.8 \mu\text{m}$ thick InP top waveguide cladding layer with doping density of $5 \times 10^{18} \text{ cm}^{-3}$; (5) a $0.2 \mu\text{m}$ thick highly doped InP top contact layer with doping density of $2 \times 10^{19} \text{ cm}^{-3}$; (6) another $0.2 \mu\text{m}$ thick highly doped InGaAs top contact layer with doping density of $2 \times 10^{19} \text{ cm}^{-3}$. The one-dimensional (in the direction perpendicular to the material layers) transverse mode profile of the waveguide structure is simulated and plotted in Fig. 2.10. Several key waveguide parameters influencing the laser performance are extracted, e.g., the effective modal refractive index is calculated to be ~ 3.255 , and the mode confinement factor Γ is estimated to be ~ 0.76 .

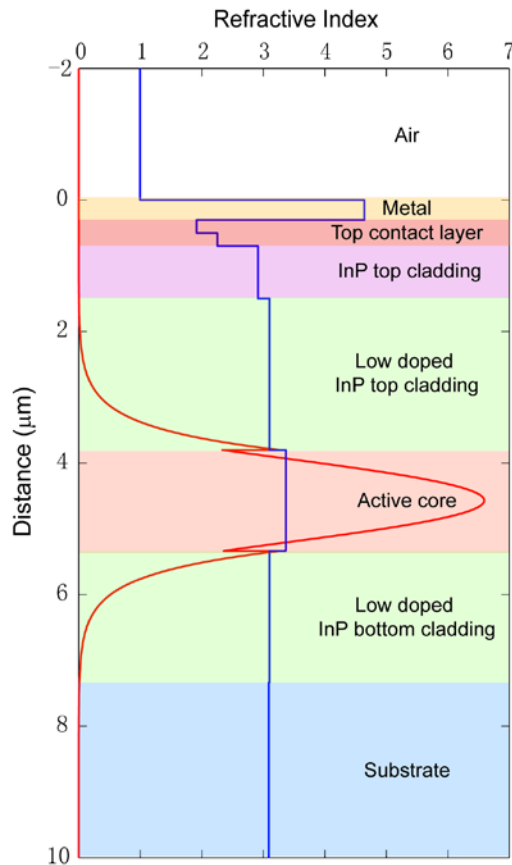


Fig. 2.10 Waveguide structure design for wafer A785 and the transverse mode profile.

2.5.3 Device fabrication

The QC laser structure is grown by MOCVD on low doped InP substrate by our collaborators at AdTech Optics. The n-type dopant incorporated in the epitaxial layers is silicon atoms. Figure 2.11 shows the doping profile in the epitaxial growth direction characterized with secondary ion mass spectroscopy (SIMS). The measured doping levels are relatively close to the designed values.

Ridge waveguide QC lasers are fabricated with ridge widths varying from 13.5–21.5 μm using conventional III-V semiconductor processing techniques. The ridges are patterned with photolithography and then wet-etched to $\sim 8 \mu\text{m}$ deep; $\sim 0.3 \mu\text{m}$ SiO_x insulation layer is deposited with plasma enhanced chemical vapor deposition (PECVD); contact windows are opened at the top of the ridges with photolithography and reactive-ion etching (RIE); contact patterns are again defined with photolithography and thin 30/300 nm Ti/Au top metal contact is deposited through electron-beam evaporation from three different angles to ensure high-quality coverage on the ridge sidewalls and corners; the substrate is then thinned down to $\sim 200 \mu\text{m}$ and 20/200 nm Ge/Au bottom metal contact is deposited through electron-beam evaporation. Circular mesa samples with diameter of $\sim 190 \mu\text{m}$ for electroluminescence (EL) and electron transport measurements are also fabricated from the same wafer with similar techniques except that no SiO_x insulation layer is applied. Ridge QC lasers with cavity lengths varying from ~ 0.5 – 4.0 mm and as-cleaved facets are mounted epitaxial-side up to copper heat-sinks. QC Lasers with buried-heterostructure waveguide and fixed cavity length of $\sim 1.9 \text{ mm}$ are also fabricated, with the back-facets coated with layers of $\text{SiO}_2/\text{Ti}/\text{Au}$ (150 nm/20 nm/150 nm, deposited through electron-beam evaporation) for high-reflectivity (HR), and mounted epitaxial-side up to copper heat-sinks. Exemplary images of fabricated devices are shown Fig. 2.12, taken with both optical microscope and scanning electron microscope (SEM).

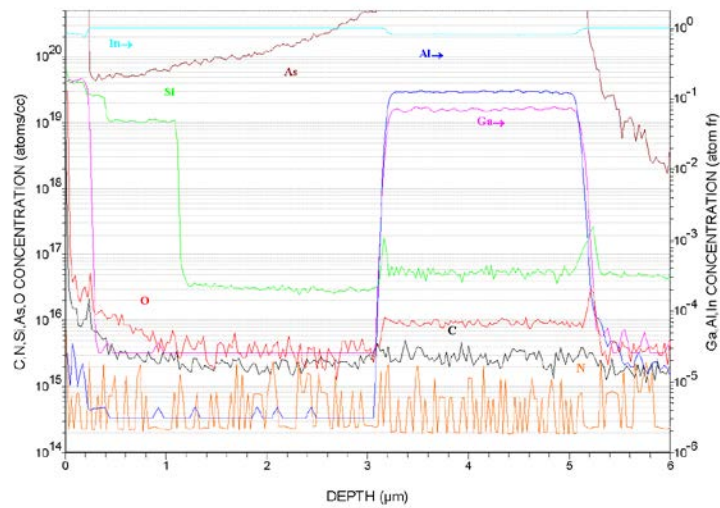


Fig. 2.11 Profiles of the material composition elements, the silicon dopant and other impurity atoms in the epitaxial layers characterized with SIMS.

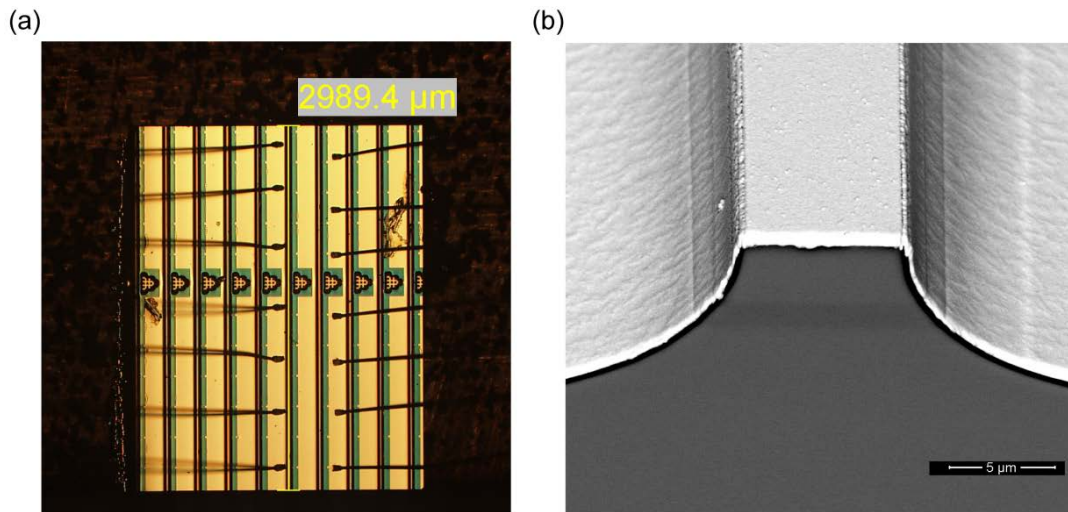


Fig. 2.12 (a) Optical microscope image of a packaged ridge waveguide QC laser chip, labeled by the optical cavity length. (b) SEM image of a QC laser as-cleaved facet.

2.5.4 Device characterization results

A large number of fabricated QC lasers with various ridge widths and lengths are fully characterized, including their lasing spectra and LIV characteristics across a wide range of temperatures. Several mesa samples cleaved into halves are also characterized for the EL spectra and IV characteristics. The spectra are measured with a Fourier transform infrared spectrometer (FTIR). The details of the experimental setups for the spectra and LIV characterizations are described in Appendix A.

Figure 2.13 shows the EL spectra of a mesa sample measured at 80 K and 300 K, respectively. The peak positions of the spectra are close to the designed transition energy. In addition, the EL spectra appear not to be significantly broadened by the ultra-strong coupling between the injector ground state and the downstream upper laser state, that their FWHM values are comparable to (slightly larger than) those of the conventional designs at similar wavelength range.

IV characteristics of the non-lasing mesa samples (Fig. 2.14) suggest significantly improved electron transport properties. This can be seen more clearly when compared to an exemplary high performance conventional design of similar wavelength and sheet doping density: the IV characteristics of the ultra-strong coupling mesa sample show both higher maximum operating current densities and lower differential resistance across a large temperature range (Fig. 2.15). Moreover, the dynamic voltage range, i.e., the difference between the turn-on voltage and the voltage at the maximum operating current density, is $\sim 45\%$ and $\sim 75\%$ of the turn-on voltage in the ultra-strong coupling design at 80 K and 300 K, respectively, compared to $\sim 28\%$ and $\sim 60\%$ in the conventional design. The difference in the turn on voltage is mainly due to the different number of stages in the two designs.

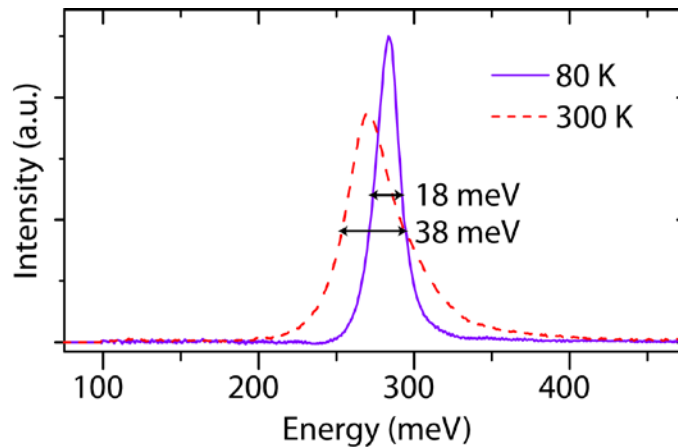


Fig. 2.13 Spectra of the EL of a mesa sample at 80 K and 300 K, respectively.

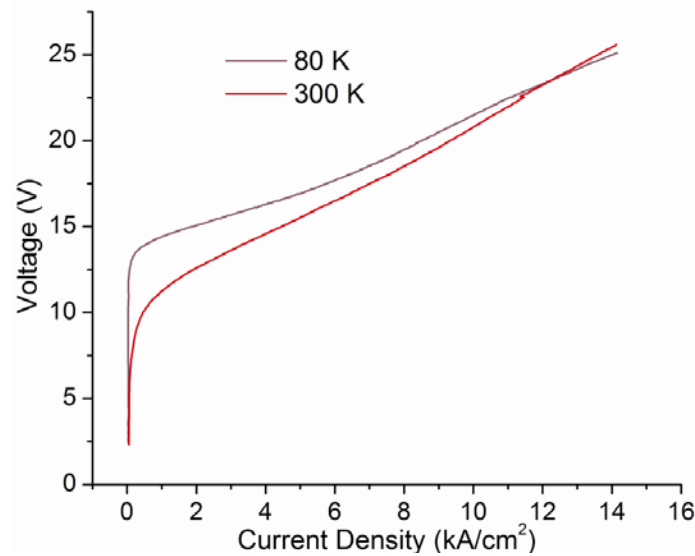


Fig. 2.14 IV characteristics for a non-lasing mesa sample at 80 K and 300 K, respectively.

The spectra of the QC lasers are characterized at various heat-sink temperatures mostly in pulsed mode operation. Representative laser spectra measured slightly above the threshold current are shown in Fig. 2.16; the lasing wavelength is $\sim 4.5 \mu\text{m}$ at 80 K and $\sim 4.7 \mu\text{m}$ at room temperature, close to the designed operating wavelength.

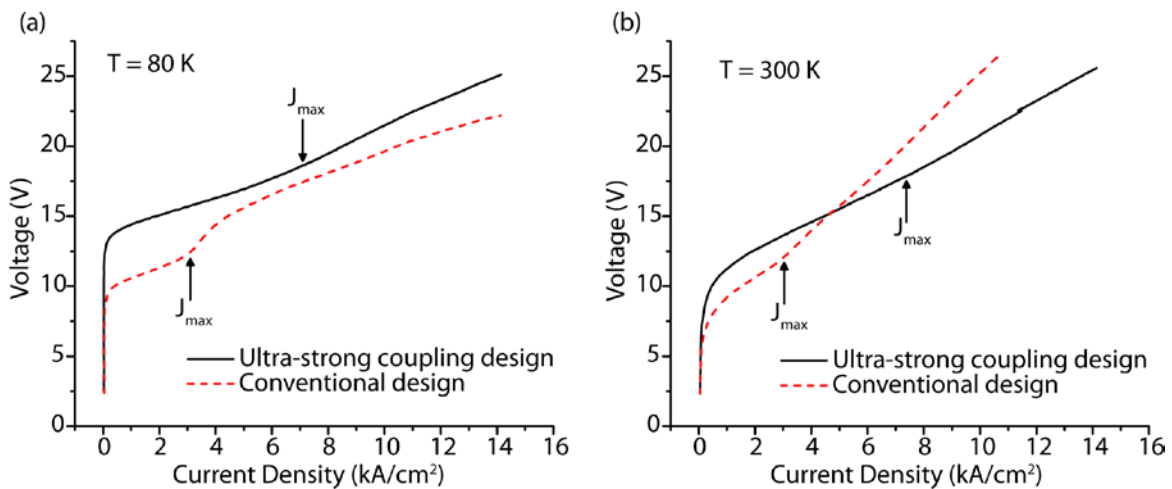


Fig. 2.15 Comparisons of electron transport properties (IV characteristics) of the ultra-strong coupling design and an exemplary conventional design of similar wavelength ($\sim 4.7 \mu\text{m}$ at 80 K) at 80 K (a) and at 300 K (b).

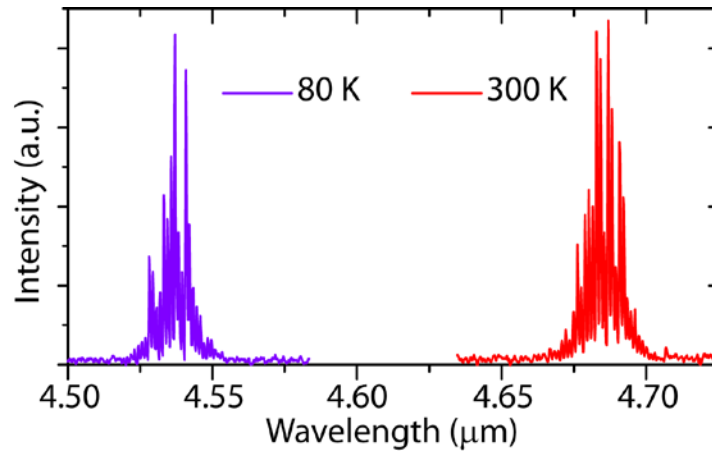


Fig. 2.16 Representative laser spectra at 80 K and 300 K.

LIV characterization results of these QC lasers show significant improvements in the device overall performance, especially in the slope efficiency, peak power level and WPE, across a broad range of temperatures compared to those of the best previously reported QC lasers at similar wavelengths and operating conditions [4,9]. Figure 2.17 shows the LIV characteristics and the calculated WPE for one of the best performing QC lasers (a 13.6 μm wide and 2.9 mm long ridge with as-cleaved facets) in pulsed mode operation (5 kHz repetition rate, 100 ns pulse width) at various heat-sink temperatures. It exhibits a high slope efficiency of ~ 8 W/A, at least ~ 10.0 W peak optical output power, and a maximum WPE of $\sim 47\%$ at 80 K. The WPE further increases to more than 48% when operated at 9 K. If taking into account the ~ 0.35 Ω measured wiring resistance from the pulse generator to the device, the WPE essentially reaches 50% at 9 K. This is a record breaking WPE at the time this work was reported and a major step forward from the previously reported best result ($\sim 34\%$) [4,9]. Even at higher temperature above 200 K, the high slope efficiency is still well maintained and the peak WPE is $\sim 35\%$ at 200 K. In order to accurately measure the output optical power, the laser beam far-field profiles (Fig. 2.18) are characterized and the optical collection efficiency of the measurement setup is calculated.

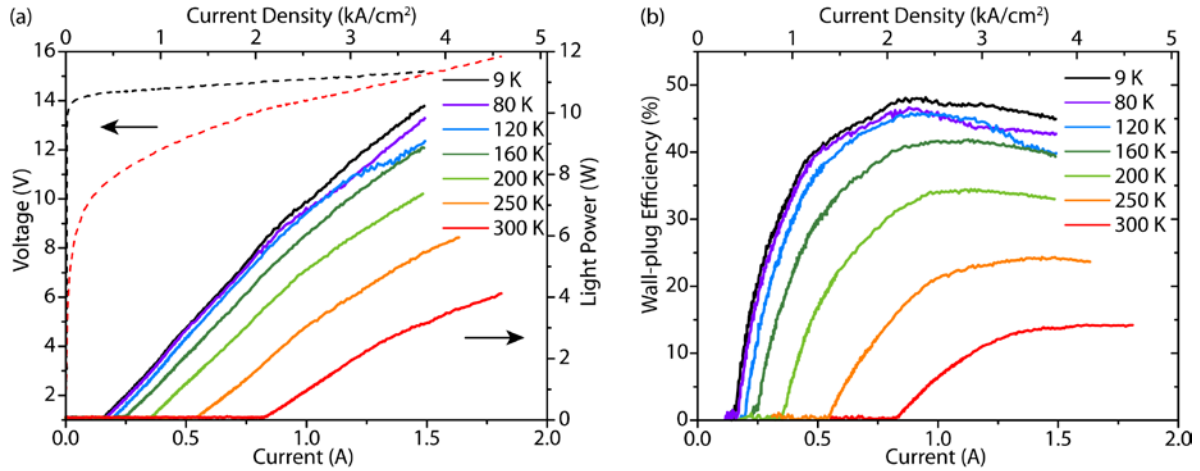


Fig. 2.17 (a) Pulsed LIV measurements for an as-cleaved $13.6 \mu\text{m}$ wide, 2.9 mm long QC laser at various heat sink temperatures as indicated. The measured single-facet optical power is doubled for two facets (a process we have tested to be valid for as-cleaved Fabry-Perot QC lasers) and corrected for the optical collection efficiency of the experimental setup (0.74, calculated from the far-field measurement of the laser in Fig. 2.18). (b) The WPE versus current is extracted from the measurement results in (a) (not corrected for the wiring resistance).

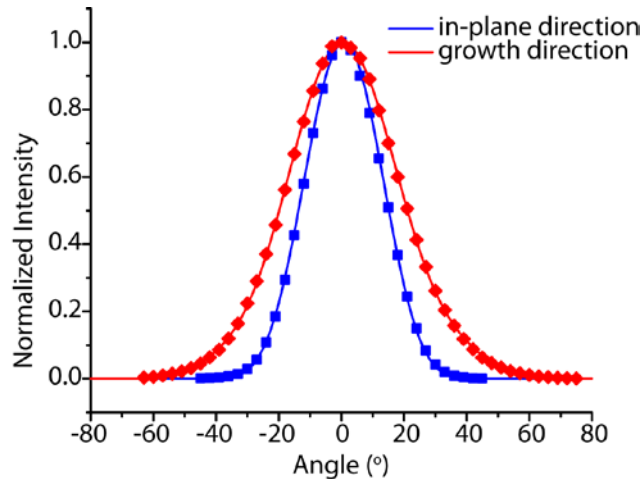


Fig. 2.18 Far-field measurements of the laser beam profiles along the growth direction and the in-plane direction. The beam divergence angles at FWHM are $\sim 41^\circ$ along the growth direction and $\sim 28^\circ$ along the in-plane direction, respectively. The symbols are the measured data points, and the lines are the corresponding fitting curves.

The high performance QC laser reported above is not an exceptional device. In fact, most of the characterized devices with similar cavity length exhibit similar high performance. Figure 2.19 shows a scatter plot of the pulsed-mode peak WPE at 80 K for all tested lasers with cavity lengths varying from $2.3\text{--}3.0 \text{ mm}$. The majority of the tested devices in this cavity length range

have a peak WPE greater than 40% at 80 K, several of them have a peak WPE greater than 45% (the data points in the plot have not been corrected for the wiring resistance). Waveguide loss of $\sim 1.5 \text{ cm}^{-1}$ is extracted from standard “1/L” measurements (Fig. 2.20), and such a relatively low waveguide loss value is also beneficial for achieving such high laser WPE. Two advantageous features of this design, i.e., the greatly improved maximum operating current density and the high slope efficiency, are maintained at high temperatures. The slope efficiency drops $< 5\%$ from 9 K to 160 K, and in the temperature range from 160 K to 300 K a very high characteristic temperature of the slope efficiency T_1 of $\sim 330 \text{ K}$ is extracted, whereas for conventional QC lasers T_1 is usually below 300 K in the same temperature range. A characteristic temperature T_0 of $\sim 125 \text{ K}$ is extracted from the threshold current density versus temperature plot in Fig. 2.21. This relatively low T_0 is suspected to be largely due to the relatively low two-LO-phonon energy defect employed for this particular design which favors low temperature operation but limits the laser threshold performance and hence the WPE at high temperature due to significant thermal back-filling effect.

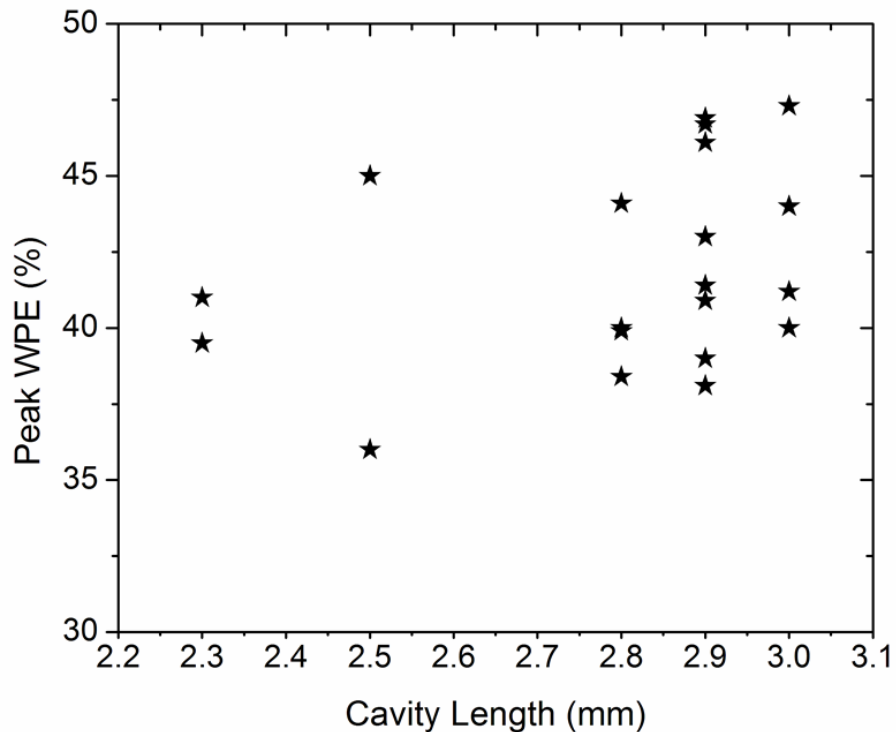


Fig. 2.19 Scatter plot of pulsed-mode peak WPE at 80 K for all tested QC lasers with various cavity lengths.

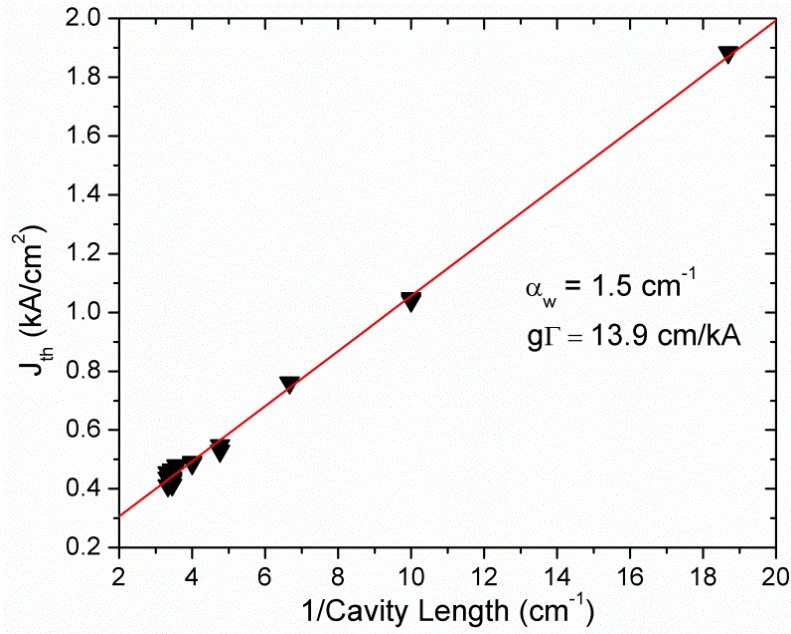


Fig. 2.20 Waveguide loss measurement at 80 K with “1/L” method. Waveguide loss of 1.5 cm⁻¹ and modal gain coefficient of 13.9 cm/kA are extracted.

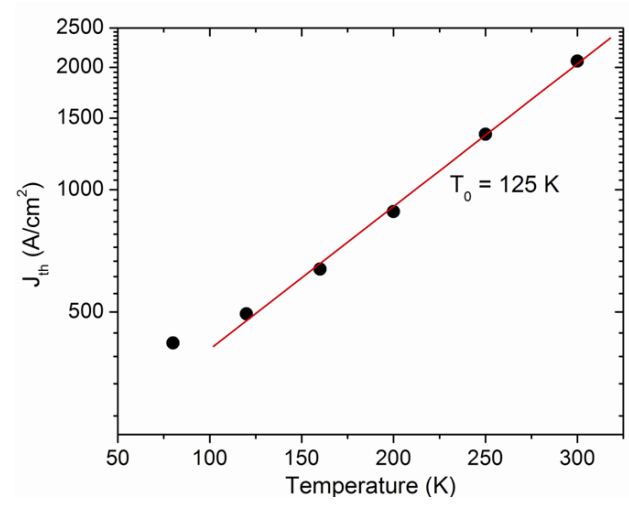


Fig. 2.21 Extraction of the characteristic temperature T_0 from the threshold current density vs. operating temperature plot. T_0 is found to be ~125 K.

These QC lasers have also been characterized in CW mode operation at cryogenic temperatures. The same laser shown in Fig. 2.17 has a peak CW power of at least 6.0 W and 4.5 W at 30 K and 80 K, respectively (Fig. 2.22(a)). Maximum values of the CW WPE of 32% at 30

K and 28% at 80 K are extracted (Fig. 2.22(b)). They are significantly lower, however, than the pulsed results at the same temperatures. This is largely due to the rapid heating-up of the laser active core as the device fabrication and packaging techniques employed are not aimed at optimizing the CW operation.

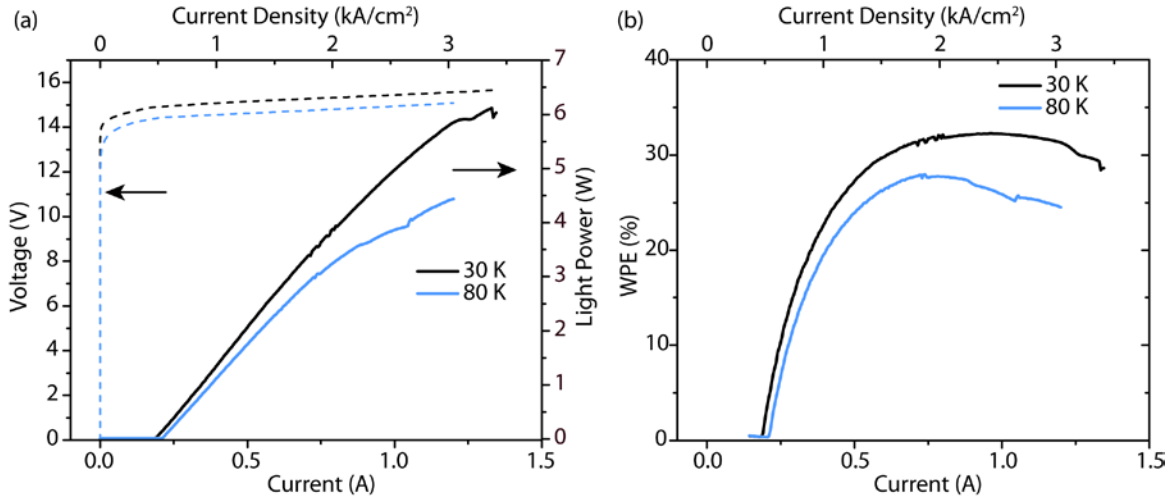


Fig. 2.22 (a) CW LIV characteristics for the same laser shown in Fig. 2.17 at heat-sink temperatures of 30 K and 80 K. The measured single-facet optical power is doubled for two facets and corrected for the optical collection efficiency of 74%. (b) The CW WPE versus current extracted from the results in (a).

QC lasers with a buried-heterostructure waveguide are also fabricated. However, these devices have limited cavity length (maximum 1.9 mm) and thus HR coating is necessary for achieving high performance. Figure 2.23 shows the pulsed LIV characteristics of a back-facet HR-coated buried-heterostructure QC laser and the calculated WPE only taking into account the optical power from the front facet. It has similar high slope efficiency ($\sim 8\text{W/A}$) and high output optical power level, and reaches $\sim 44\%$ WPE at 80 K and $\sim 16\%$ at 300 K. Figure 2.24 shows its CW LIV characteristics, which exhibits an improved CW performance in terms of usable optical power level, maximum operating temperature (230 K) compared to the simple ridge QC lasers. The CW performance is expected to be further improved with more advanced fabrication processes (e.g. thick electro-plated gold for top contact) and/or packaging techniques (e.g. epitaxial-side down mounting, diamond heat-sink) for faster heat removal.

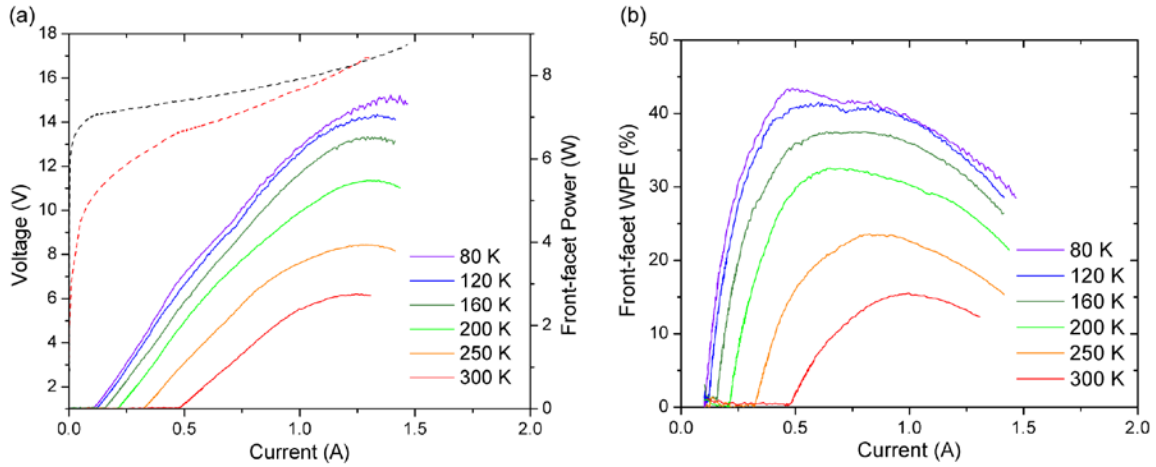


Fig. 2.23 (a) Pulsed LIV characteristics for a buried-heterostructure QC laser ($14\ \mu\text{m}$ wide and $1.9\ \text{mm}$ long) with back-facet HR coating at various heat-sink temperatures. Optical power is only measured from the front-facet, and is corrected for optical collection efficiency of 74%. (b) The pulsed WPE versus current extracted from the experimental results in (a).

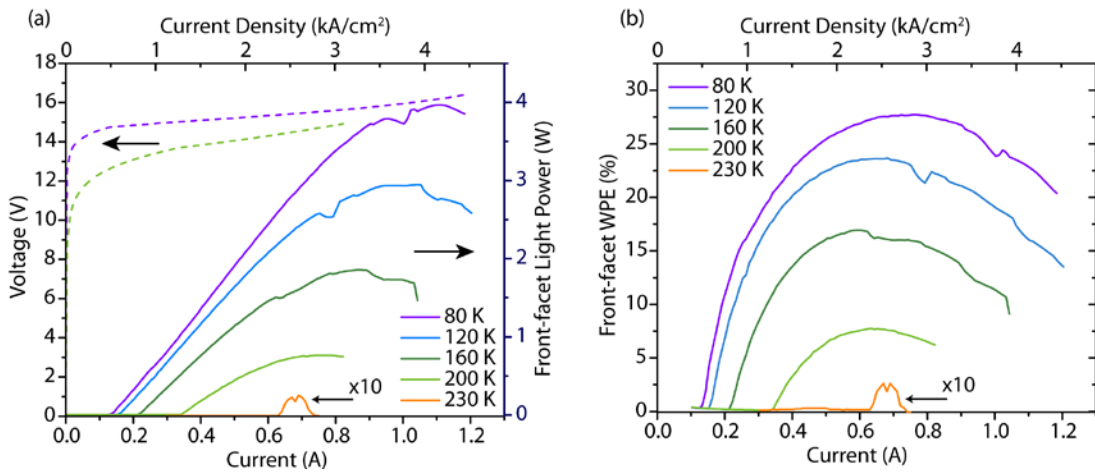


Fig. 2.24 (a) CW LIV characteristics for the same laser in Fig. 2.23 at various heat-sink temperatures. Optical power is only measured from the front-facet, and is corrected for optical collection efficiency of 74%. (b) The CW WPE versus current extracted from the experimental results in (a).

To summarize this section, we have experimentally realized a new QC laser design employing ultra-strong coupling between the injector ground state and the downstream upper laser state. The significantly increased coupling strength effectively overcomes the interface-roughness-induced dephasing of the resonant tunneling process and facilitates the electron transport, which in turn greatly improves the QC laser performance, such as the slope efficiency, the output optical power and especially the WPE. An unprecedented $\sim 50\%$ WPE is experimentally demonstrated.

2.6 Ultra-strong coupling QC lasers with broad-band optical gain

In addition to improving the power performance of QC lasers, the ultra-strong coupling design strategy can also be exploited to achieve broad-band optical gain, which is highly interesting for applications such as multi-species molecular sensing, spectrometer sources and frequency combs in mid-IR wavelength range. Three features associated with the ultra-strong coupling regime offer the potential for realizing broad optical gain spectrum. First of all, according to Eqn. (2.43) the broadening of the radiative transition between the upper laser state and the lower laser state tends to be larger for ultra-strong coupling designs because the upper laser state partially extends into the injector region and experience more interfaces that are not seen by the lower laser state. Secondly, the injector ground state is strongly coupled with the downstream upper laser state and therefore also has significant contribution to the radiative transition. The broadening of the transition between the injector ground state and the lower laser state is expected to be large because of their small spatial overlap. Last but not least, the larger coupling strength introduces a larger energy splitting between the two anti-crossed states which directly adds to the optical gain spectrum width. In fact, the three factors are all reflected in Eqn. (2.53) for the optical gain calculation based on the density matrix model. Moreover, more than two states can be strongly coupled to further broaden the optical gain spectrum [29,30]. In this section, a QC laser design employing both ultra-strong coupling and short injector design strategies is presented, with which an exceedingly broad-band optical gain is realized.

2.6.1 Band-structure design

Figure 2.25 shows the band-structure design with the wavefunctions of the eigenstates associated with the entire periodic structure plotted. The entire band-structure design makes use of strain balanced InGaAs/AlInAs material system to provide large enough band-offset for the relatively short wavelength operation. The designed materials compositions are $\text{In}_{0.62}\text{Ga}_{0.38}\text{As}/\text{Al}_{0.70}\text{In}_{0.30}\text{As}$, and the corresponding band-offset is ~ 870 meV. The three states in red extending through an entire period are strongly coupled with each other and all contribute to the optical gain. The lower laser state is plotted in blue. The radiative transition energy is designed to be ~ 210 meV, corresponding to an emission wavelength of ~ 6 μm . The active region makes use of two resonant LO-phonons depopulation scheme, and the total energy defect is designed to be ~ 85 meV.

The origin of the 3 strongly coupled upper laser states can be seen more clearly from Fig. 2.26, which plots the wavefunctions of the eigenstates associated with the bases. Here, one stage of the QC structure is divided in two bases: the active region and the short injector, and the boundaries between them are shown in the red dashed lines. The injector ground state (plotted in green) couples to both the excited state in the downstream active region (plotted in red) and the lowest ground state in the upstream active region (plotted in purple), with calculated coupling strength of 10.9 meV and 9.5 meV, respectively, belonging to the ultra-strong coupling regime. Due to the compactness of the injector, the 3 states couple to each other simultaneously and form

the 3 extended upper laser states. The width of the optical gain for such a design is expected to be much larger than that for a conventional design with the upper laser state localized in the active region.

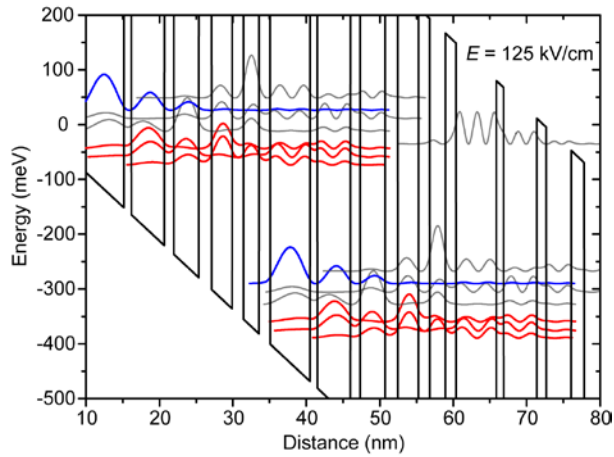


Fig. 2.25 Band-structure of the broad-band optical gain ultra-strong coupling QC laser design (wafer No. A1392).

Starting from the widest quantum well, the layer sequence of one period of the active region/injector pair in the electron downstream direction with individual thickness in nanometer is: 5.45/**1.0**/4.5/**1.3**/3.4/**1.75**/2.8/**1.55**/2.1/**1.5**, where the InAlAs barrier layers are in bold, the InGaAs well layers are in roman. The underlined layers are doped with a bulk doping density of $2.2 \times 10^{17} \text{ cm}^{-3}$, corresponding to a sheet doping density of $\sim 1 \times 10^{11} \text{ cm}^{-2}$ per period.

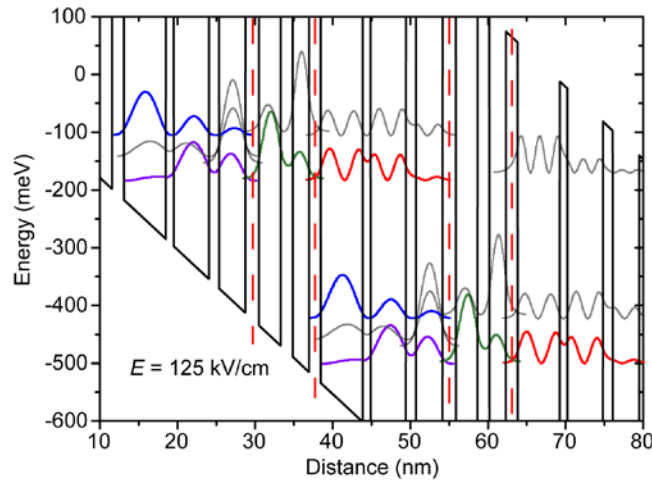


Fig. 2.26 Band-structure of the same design in Fig. 2.25 with the localized wavefunctions in the divided bases plotted. One period of active region/injector pair is divided into 2 bases at the barriers indicated by the red dashed lines.

2.6.2 Waveguide design

The active core of this QC laser design contains 50 periods of active region/injector pairs with a total thickness of $\sim 1.3 \mu\text{m}$. The waveguide structure is designed to have the following structure: from the substrate up, the layers sequence is (1) a $2 \mu\text{m}$ thick InP bottom waveguide cladding layer with low doping density of $2.0 \times 10^{16} \text{ cm}^{-3}$; (2) the $1.3 \mu\text{m}$ thick active core with average doping density of $3.8 \times 10^{16} \text{ cm}^{-3}$; (3) a $2.5 \mu\text{m}$ thick InP top waveguide cladding layer with low doping density of $2 \times 10^{16} \text{ cm}^{-3}$; (4) an additional $0.8 \mu\text{m}$ thick InP top waveguide cladding layer with doping density of $5 \times 10^{18} \text{ cm}^{-3}$; (5) a $0.1 \mu\text{m}$ thick highly doped InP top contact layer with doping density of $2 \times 10^{19} \text{ cm}^{-3}$; (6) another $0.1 \mu\text{m}$ thick highly doped InGaAs top contact layer with doping density of $2 \times 10^{19} \text{ cm}^{-3}$. The one-dimensional (in the direction perpendicular to the material layers) transverse mode profile of the waveguide structure is simulated and plotted in Fig. 2.27. Several key waveguide parameters influencing the laser performance are extracted, e.g., the effective modal refractive index is calculated to be ~ 3.195 , and the mode confinement factor Γ is estimated to be ~ 0.54 . It should also be noticed in Fig. 2.27 that the transverse mode is weakly coupled into the surface plasmon mode in the highly doped top contact layer, and therefore would incur higher waveguide loss.

2.6.3 Device characterization results

The QC laser structure is grown by MOCVD on low doped InP substrate by our collaborators at AdTech Optics. Ridge waveguide QC lasers with various ridge widths and lengths and circular mesa samples for EL and electron transport measurements are fabricated and packaged using the same processes described in the previous section. The devices are then fully characterized for their spectral and LIV (IV for non-lasing mesa samples) characteristics.

The EL from non-lasing half-circular mesa samples is characterized and indeed exhibit very broad spectra across the entire operating temperature range from 80 K to 300 K. Figure 2.28(a) shows the EL spectra measured at current density of 1 kA/cm^2 and at 80 K, 200 K, and 300 K, respectively. The FWHM of the EL spectra at various temperatures are plotted in Fig. 2.28(b), together with the information of the percentage of the transition energy the spectra width corresponds to. At 80 K, the FWHW of the EL spectra corresponds to $\sim 30\%$ of the transition energy, and it increases almost linearly to $\sim 40\%$ at 300 K. Such values are much larger than what is usually achieved with conventional QC laser designs, and are comparable to the state-of-the-art broad-band optical gain QC laser designs ($\sim 40\%$) [31].

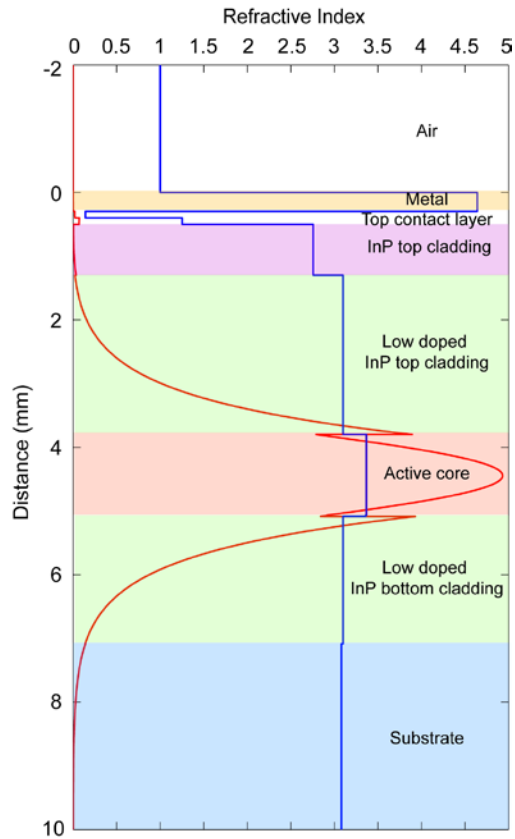


Fig. 2.27 Waveguide structure design for wafer A1392 and the transverse mode profile.

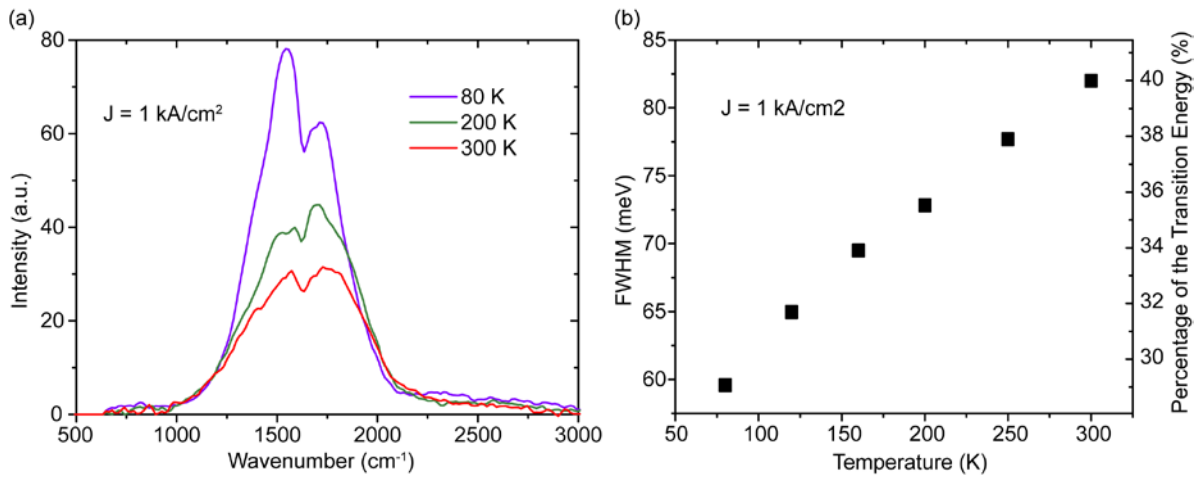


Fig. 2.28 (a) EL spectra measured from a half-circular mesa operated at 1 kA/cm^2 current density and various temperatures. (b) FWHM of the EL spectra at various operating temperatures and the percentage of the transition energy they correspond to.

The IV characteristics of non-lasing mesa samples are characterized (Fig. 2.29) and show similar features as those of the ultra-strong coupling design (A785) described in Section 2.6, including low differential resistance, large operating current density and voltage range (up to current density of more than 10 kA/cm^2 , no obvious kink or increase of differential resistance is observed in the IV curves), which indicate good electron transport property.

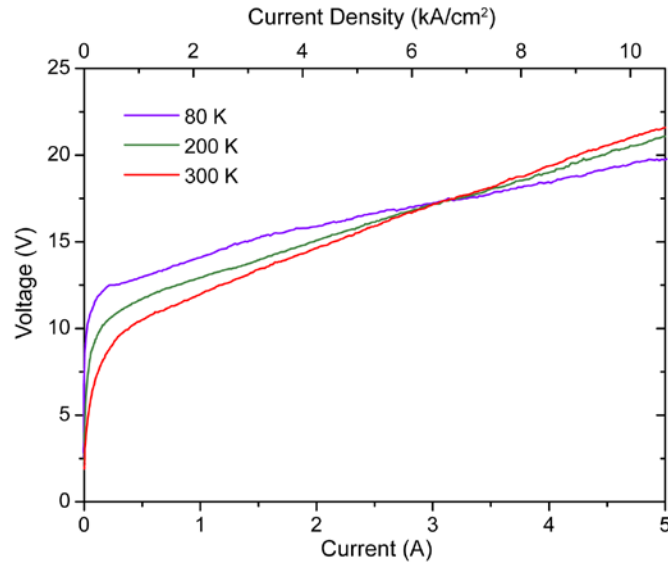


Fig. 2.29 IV characteristics for a circular non-lasing mesa at various operating temperatures.

Representative laser spectra at 80 K and 300 K are shown in Fig. 2.30. The emission wavelength at 80 K is slightly longer than the designed value, and it is abnormally red-shifted in comparison with the emission wavelength at 300 K (for most QC laser designs the emission wavelength red-shifts with increasing temperature). The discrepancy of the emission wavelength from its designed value and the unusual temperature dependence of the emission wavelength may be attributed to the relatively early turn-on of the current flow as a result of the ultra-strong coupling and the short injector employed.

Figure 2.31 shows the LIV characteristics of a representative laser and the calculated WPE in pulsed mode operation across a large temperature range. From the threshold voltage, the electric field applied across the device structure is $\sim 100 \text{ kV/cm}$, much lower than the designed electric field ($\sim 125 \text{ kV/cm}$) for the three strongly coupled states to be in full resonance. Compared to the high performance QC lasers in the previous section, the threshold current density at 80 K for these QC lasers operating at $\sim 6.3 \mu\text{m}$ is higher and also increases faster with temperature, corresponding to a low characteristic temperature of $\sim 107 \text{ K}$ (Fig. 2.32). The higher threshold current density can be attributed to both a lower waveguide mode confinement factor ($\Gamma \approx 0.54$) which limits the modal gain and a higher waveguide loss of $\sim 5.3 \text{ cm}^{-1}$ (Fig. 2.33).

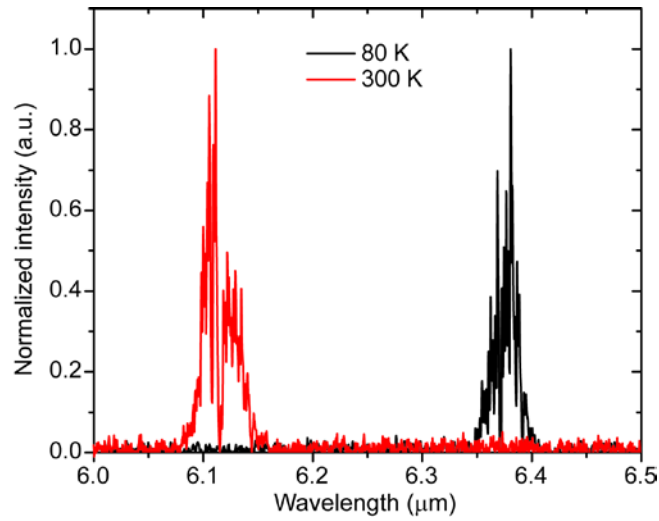


Fig. 2.30 Representative laser spectra at 80 K and 300 K.

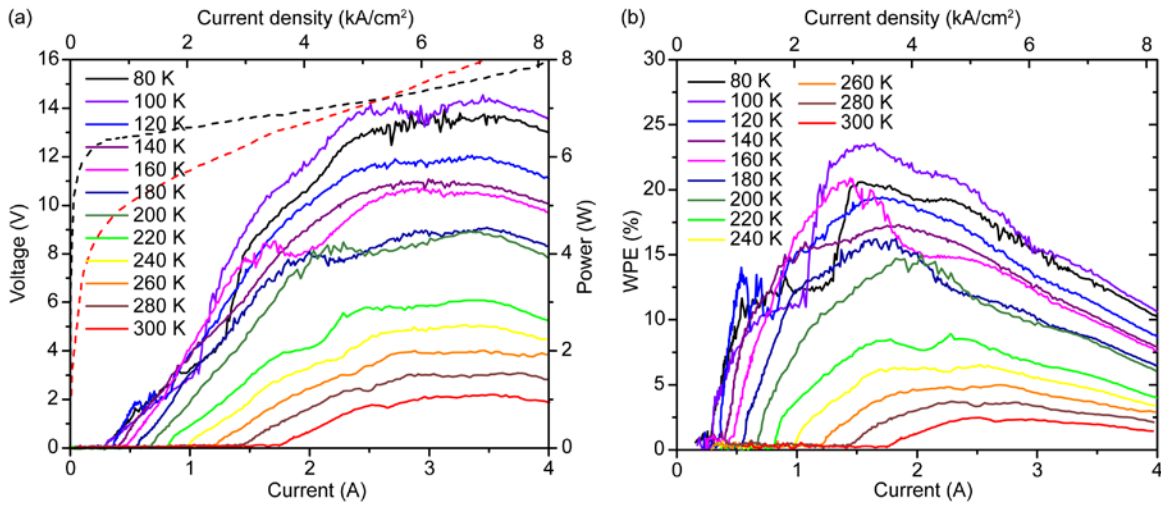


Fig. 2.31 (a) Pulsed LIV characteristics for a representative QC laser (3 mm long and 16.3 μm wide ridge) at various heat-sink temperatures. (b) WPE calculated from the experimental results in (a).

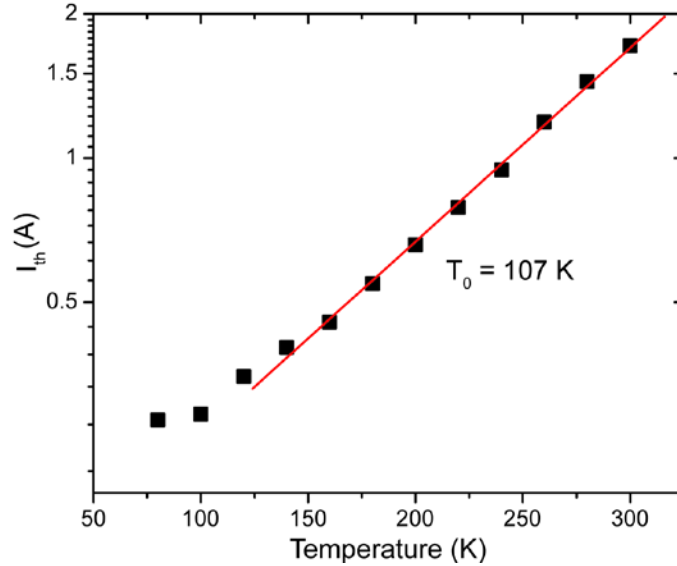


Fig. 2.32 Characteristic temperature T_0 (~ 107 K) extracted from the threshold current versus operating temperature plot.

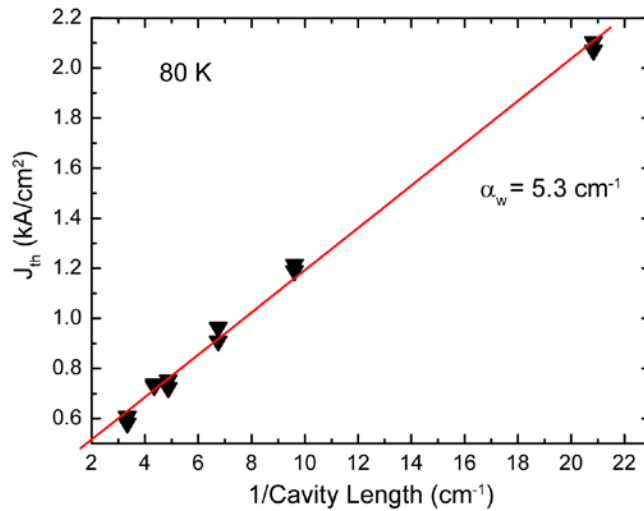


Fig. 2.33 Waveguide loss at 80 K extracted with the “1/L” method.

The waveguide loss is extracted with standard “1/L” method at 80 K and is found to be ~ 5.3 cm⁻¹, much higher than that of the high performance wafer A785, which in turn can be attributed to the longer emission wavelength (free carrier absorption is proportional to the emission wavelength squared) and the weak coupling of the transverse mode to the surface plasmon mode in the highly doped top contact layer as can be seen in Fig. 2.27. This relatively large waveguide loss is a significant limiting factor for the QC laser performance, including the

threshold current density, the slope efficiency, the optical power level as well as the maximum WPE that can be achieved. The overall performance for this QC laser design is expected to be further improved with a more optimized waveguide design.

The characteristic temperature T_0 for both the high performance ultra-strong coupling design in the previous section and the broad-band optical gain design employing ultra-strong coupling and short injector reported above are relatively low compared to state-of-the-art conventional QC lasers, and considerably limit the device performance at high temperatures (e.g. room temperature) and in CW mode, which are highly desired for many real-world applications. In both designs, the energy defects employed between the lower laser state and the injector ground state are relatively low compared to those of the best performing conventional QC laser designs, leading to more severe thermal backfilling when operated at high temperatures. This may well be a contributing factor for the relatively low T_0 . In addition, for the broad-band optical gain design, the laser slope efficiency also deteriorates relatively fast with increasing temperature, indicating other mechanisms such as significant carrier leakage may also play a role in limiting the device performance at high temperatures. How to further improve the device performance at high temperature is a key question. In the next section, systematic and comparative study on the performance of a number of different ultra-strong coupling QC lasers are presented, with an emphasis on factors influencing the temperature performance.

2.7 Influence of taller electron exit barriers on the temperature performance of ultra-strong coupling QC lasers

Besides the two reported in the previous two sections, we have implemented the ultra-strong coupling design strategy in a number of other QC laser designs (12 designs in total, see Appendix B) mostly in the wavelength range of 4 μm to 5 μm . They are designed for different purposes and have differences in various aspects of the band-structure. Some of them perform better than the others. By comparing the device performance and certain device parameters across some or all the designs, we can gain insight on which parameters have higher impact on the device performance and how to adjust them to further improve the device performance.

One of the most important goals for our design exploration is to identify the major causes for the relatively low characteristic temperatures observed in several ultra-strong coupling designs and find out effective ways to improve the characteristic temperatures. If the waveguide loss does not change with temperature significantly, then a relatively low characteristic temperature is a result of relatively fast degrading of the population inversion with increasing temperature. There are two major causes for such temperature dependent population inversion degradations: thermal backfilling of electrons from the injector ground state to the lower laser state and electron leakage from the upper laser state due to thermal excitation. In order to investigate the influence of these two factors on the temperature performance of ultra-strong coupling QC lasers, we design two pairs of ultra-strong coupling QC lasers with contrasting features. The first pair of designs employs the two resonant LO-phonons depopulation scheme while the second pair employs the three resonant LO-phonons depopulation scheme, and therefore the energy defect is

different for the two pair of designs. By comparing the temperature performance between the two pairs of designs, we expect to see whether the thermal backfilling is a significant factor limiting the laser characteristic temperature. Within each pair, the two designs are almost identical except for the two barriers after the active region which we refer to as the electron exit barriers. The difference is that the electron exit barriers in one design are made taller by changing the material composition, and such taller barriers have been demonstrated to be capable of suppressing the electron leakage into the continuum states above the barriers [32,33], therefore comparisons between the baseline design and the taller-barrier design would provide us with information on the influence of the electron leakage into the continuum on the characteristic temperature.

2.7.1 Band-structure designs

The pair of two-LO-phonon designs are shown in Fig. 2.34 and the pair of three-LO-phonon designs are shown in Fig. 2.35. The baseline two-LO-phonon design has a radiative transition energy of ~ 255 meV and an energy defect of ~ 82 meV. The coupling strength between the injector ground state and the downstream upper laser states is ~ 17 meV. Starting from the widest quantum well, the layer sequence of one period of the active region/injector pair in the electron downstream direction with individual thickness in nanometer is:

4.2/**1.2**/3.9/**1.4**/3.3/**2.25**/3.05/**2.2**/2.4/**2.0**/1.8/**1.8**/1.5/**1.3**/1.2/**1.0**, where the $\text{In}_{0.31}\text{Al}_{0.69}\text{As}$ barrier layers are in bold, the $\text{In}_{0.66}\text{Ga}_{0.34}\text{As}$ well layers are in roman. The underlined layers are doped with a bulk doping density of $2.0 \times 10^{17} \text{ cm}^{-3}$, corresponding to a sheet doping density of $8.8 \times 10^{10} \text{ cm}^{-2}$ per period. In the taller-barrier two-LO-phonon design, the middle parts of two electron exit barriers are made taller by ~ 240 meV ($\text{In}_{0.11}\text{Al}_{0.89}\text{As}$), while the rest of the design details are identical to the baseline design. The baseline three-LO-phonon design has a radiative transition energy of ~ 260 meV and an energy defect of ~ 122 meV. The coupling strength between the injector ground state and the downstream upper laser states is ~ 16 meV. Starting from the widest quantum well, the layer sequence of one period of the active region/injector pair in the electron downstream direction with thickness in nanometer is:

4.15/**0.9**/3.8/**1.1**/3.25/**1.1**/2.9/**1.8**/2.35/**1.45**/2.05/**1.45**/1.75/**1.45**/1.55/**1.45**/1.45/**1.15**, where the $\text{In}_{0.21}\text{Al}_{0.79}\text{As}$ barrier layers are in bold, the $\text{In}_{0.68}\text{Ga}_{0.32}\text{As}$ well layers are in roman. The underlined layers have a bulk doping density of $1.0 \times 10^{17} \text{ cm}^{-3}$, corresponding to a sheet doping density of $7.3 \times 10^{10} \text{ cm}^{-2}$ per period. In the taller-barrier three-LO-phonon design, the two electron exit barriers are made taller by ~ 130 meV ($\text{In}_{0.12}\text{Al}_{0.88}\text{As}$), while the rest of the design details are identical to the baseline design.

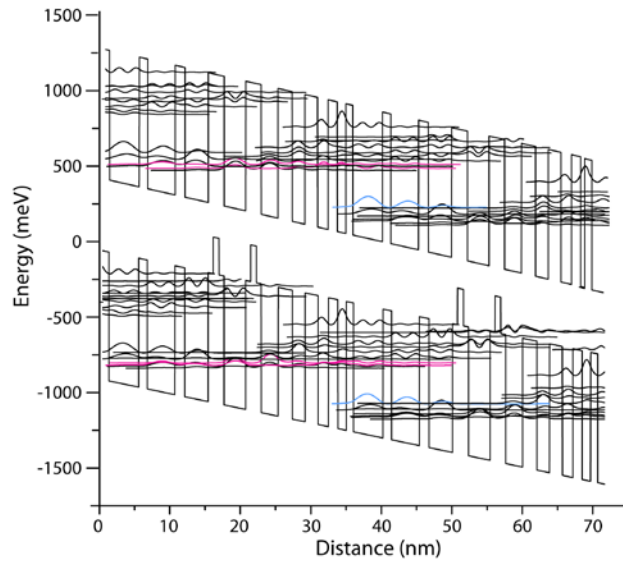


Fig. 2.34 Band-structures for the pair of two-LO-phonon designs. The top one is the base line design (wafer No. A1641) while the bottom one is the taller-barrier design (wafer No. A1643).

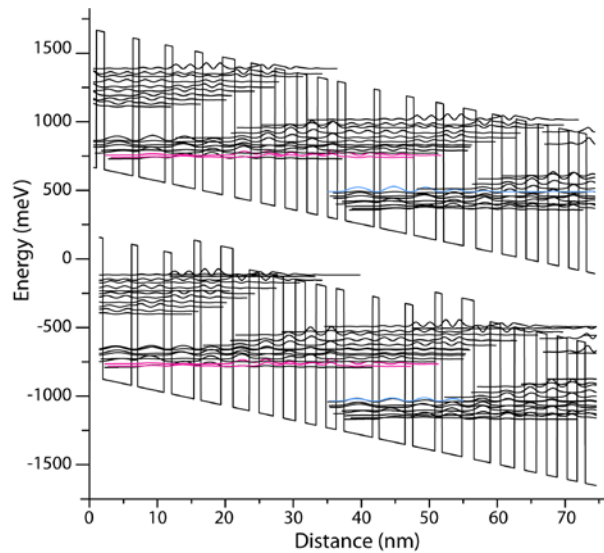


Fig. 2.35 Band-structures for the pair of three-LO-phonon designs. The top one is the base line design (wafer No. A1637) while the bottom one is the taller-barrier design (wafer No. A1639).

2.7.2 Device characterization results

The two pairs of QC laser designs are grown by MOCVD on low doped InP substrate by our collaborators at AdTech Optics back-to-back to ensure similar growth quality. QC lasers and circular mesa samples from the four wafers are fabricated with standard processes described

previously. The comparisons of the EL spectra within each pair of designs are shown in Fig. 2.36 (two-LO-phonon designs) and Fig. 2.37 (three-LO-phonon designs), respectively.

As shown in Fig. 2.36 and Fig. 2.37, the peak positions of the EL all accurately match the designed radiative transition energies. For the two designs of either pair, the spectra of their EL at the same current density are very similar at both 80 K and 300 K, though the width for the EL spectra of the taller-barrier designs are mostly slightly larger than those for the baseline designs for both pairs. The broader EL spectra associated with the taller-barrier designs can be explained by the stronger interface roughness induced broadening effect to the radiative transitions as a result of the larger band offset at the taller barriers. However, the EL spectrum of the three-LO-phonon taller-barrier design at 80 K (but not at 300 K) is considerably broader than its baseline counterpart, and the underlying cause is unclear.

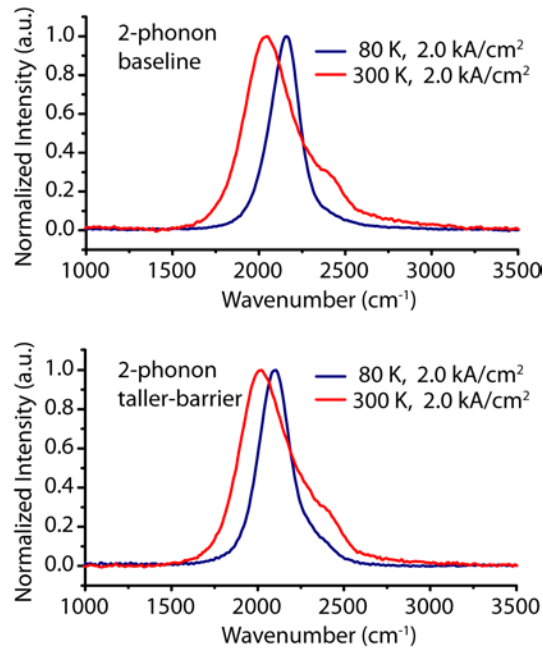


Fig. 2.36 EL spectra for the two-LO-phonon baseline design (top) and the two-LO-phonon taller-barrier design (bottom) at 80 K and 300 K.

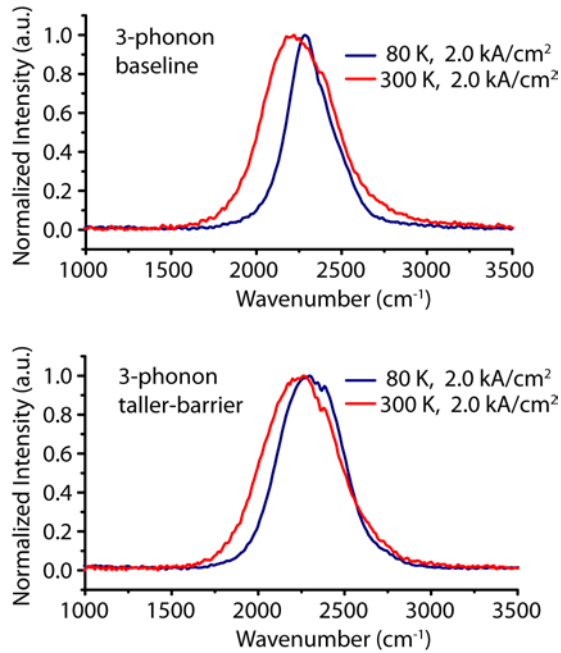


Fig. 2.37 EL spectra for the three-LO-phonon baseline design (top) and the three-LO-phonon taller-barrier design (bottom) at 80 K and 300 K.

The representative LIV characteristics for QC lasers from 4 different designs are shown in pairs in Fig. 2.38 (two-LO-phonon designs) and Fig. 2.39 (three-LO-phonon designs), together with the extracted values for their characteristic temperature T_0 . Comparing the LIV characteristics in Fig. 2.38 (a) and (c), we see that the two-LO-phonon baseline design and the taller-barrier design have similar performance in terms of threshold current density and slope efficiency (the maximum output optical power cannot be directly compared due to the difference in ridge widths) at cryogenic temperatures (e.g. 80 K), while at room temperature the taller-barrier design has moderately lower threshold current density and higher slope efficiency, and at 390 K the taller-barrier design has much better performance. The characteristic temperature of the taller-barrier design is ~ 30 K higher than that of the baseline design (163 K vs. 133 K). Comparing the LIV characteristics in Fig. 2.39 (a) and (c), we see that the three-LO-phonon taller-barrier design has much better slope efficiency than the baseline design across the entire temperature range. However, the baseline design has a lower threshold current density at 80 K, but its threshold current density increases relatively faster with temperature than that of the taller-barrier design. The characteristic temperature of the taller-barrier design is also ~ 30 K higher than that of the baseline design (181 K vs. 152 K). Therefore, in both cases the characteristic temperatures are increased by ~ 30 K with taller electron exit barriers. Such a large difference in the characteristic temperatures suggests that the electron leakage into continuum states through thermal excitation can be significant in these ultra-strong coupling designs, and employing taller electron exit barriers is an effective way of suppressing such an electron leakage path and improve the device high temperature performance.

On the other hand, the characteristic temperatures for the pair of three-LO-phonon designs are higher than those of the pair of two-LO-phonon designs by ~ 20 K. This observation indicates that the thermal backfilling effect also plays a non-negligible role in limiting the device temperature performance at least for the two-LO-phonon designs. Therefore, for future optimizations of the ultra-strong coupling designs aiming at better high temperature performance, both design strategies investigated above, taller electron exit barriers and larger energy defect, may prove to be effective if properly incorporated.

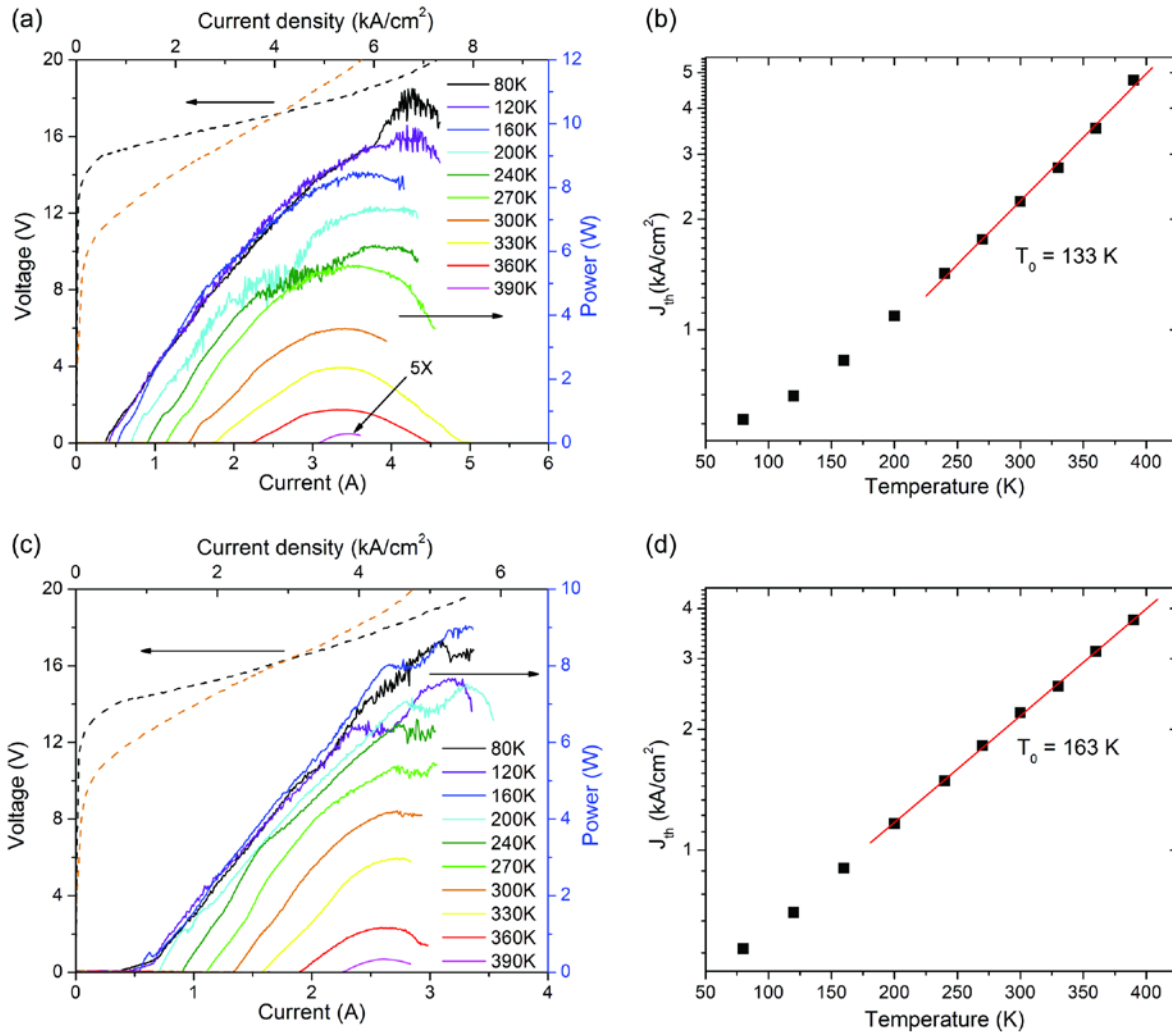


Fig. 2.38 Representative QC laser LIV characteristics for the two-LO-phonon baseline design (a) and the taller-barrier design (c), together with the extracted characteristic temperatures (b) and (d).

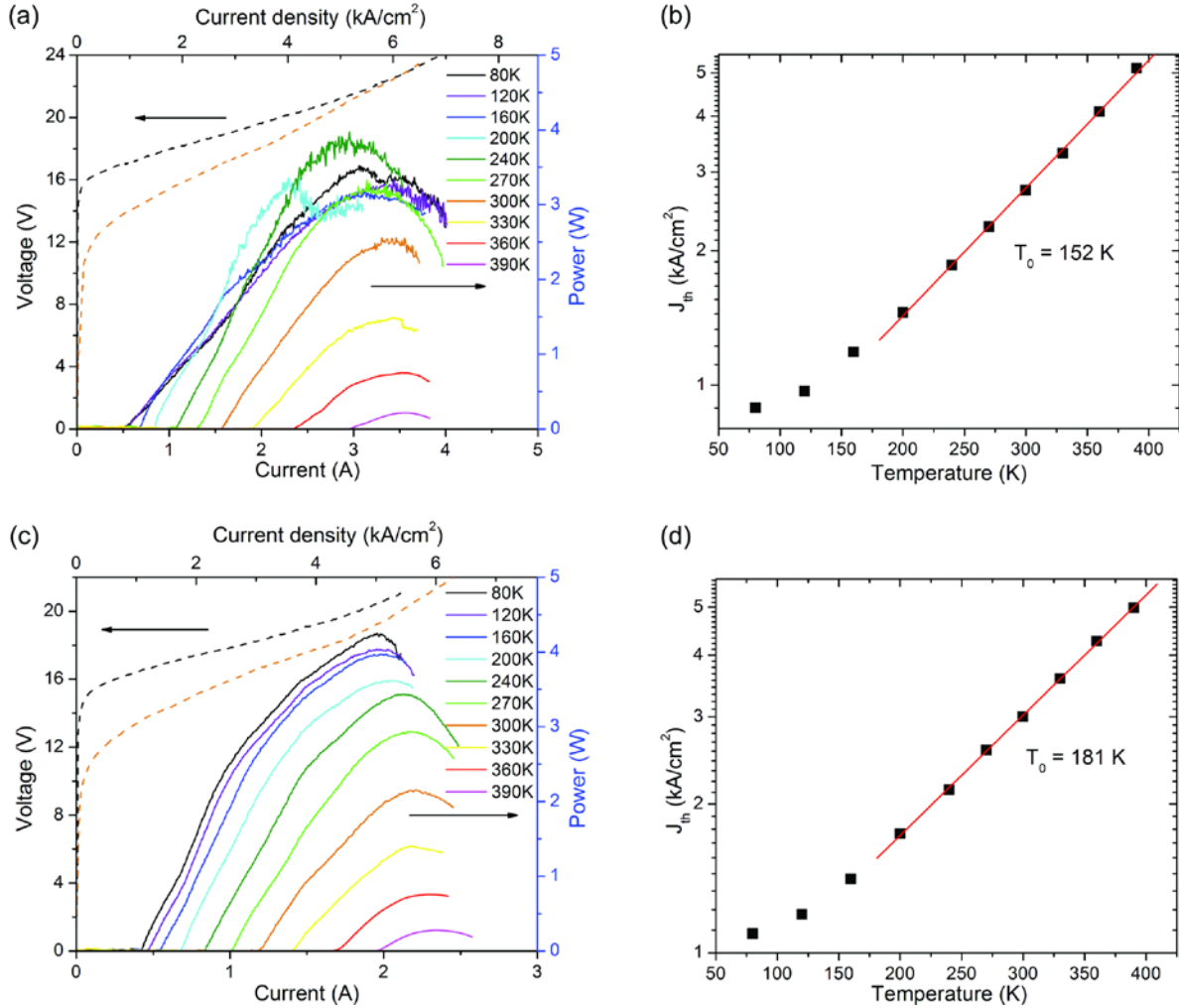


Fig. 2.39 Representative QC laser LIV characteristics for the three-LO-phonon baseline design (a) and the taller-barrier design (c), together with the extracted characteristic temperatures (b) and (d).

2.8 Conclusions and discussions

In this chapter we have first derived the WPE expression for QC lasers and analyzed the crucial impact of the electron transport property on the QC laser overall performance. Then we have reviewed several major electron transport processes in QC lasers and studied in depth the resonant tunneling process based on the density matrix formalism. We have found that due to the strong dephasing in connection with the interface roughness induced intrasubband scattering, the resonant tunneling process between the injector ground state and the downstream upper laser state is likely the bottleneck for the electron transport through the device. Such an interface roughness induced dephasing effect was long underestimated in conventional QC laser design, that the coupling strength employed in most conventional QC laser designs was not sufficient to effectively overcome its negative influence on the resonant tunneling process. Therefore, we

have proposed to employ a much larger coupling strength in QC laser band-structure designs which we refer to as the ultra-strong coupling design strategy, and calculated the optimal coupling strength with our density matrix based model. By implementing the ultra-strong coupling design strategy in real QC lasers, we have demonstrated a major step forward in the overall device performance and achieved a record breaking QC laser WPE of ~50%. In addition, this design strategy has been applied to realization of QC lasers with exceedingly broad optical gain. We have further explored different design strategies combined with the ultra-strong coupling to effectively improve the temperature performance of these QC lasers.

It is worth pointing out that the optimal coupling strength is critically dependent on certain material parameters such as the interface roughness average height and correlation length, etc. These material parameters are mostly determined by the epitaxial growth technology employed. Therefore, if the epitaxial growth technologies further improve, the optimal coupling strength would also change accordingly. Of course, the optimal coupling strength also depends on the material systems used, especially on the values of the band offset.

The large number ultra-strong coupling designs we implemented also allow us to cross compare their performance and identify certain key parameters whose influence on the device performance would be difficult to extract from individual designs. For example, we have observed that the energy difference between the upper laser state and the band edge of the lowest satellite valleys (L-valleys for these designs) of the quantum well material (ΔE , see Fig. 2.40) may have a significant impact on the optical gain coefficient. Such an observation is obtained by comparing the performance of 11 different ultra-strong coupling designs with emission wavelengths in the range of ~4 μm to 5 μm . (The wafer No. for these 11 designs are A728, A785, E109318, A1015, A1162, A1390, M1065, A1637, A1639, A1641 and A1643. See Appendix B for details of these designs.) Despite the similar operating wavelengths, comparable coupling strengths and almost identical waveguide structures employed, the 11 different designs exhibit a wide range of modal gain coefficients (extracted from standard “1/L” method at 80 K) and FWHM of the optical gain spectra. If assuming the electron injection efficiency is unity, then the gain coefficient at the peak of the optical gain spectrum satisfy the expression [34]

$$g = \frac{\text{FOM}}{L_p \cdot \gamma_{32}}, \quad (2.56)$$

where L_p is the thickness of one period of the active region/injector pair, γ_{32} is the FWHM of the optical gain spectra, and FOM is the figure of merit associated with the design and is defined as

$$\text{FOM} = \tau_3 \left(1 - \frac{\tau_2}{\tau_{32}}\right) \frac{8\pi e z_{32}^2}{\epsilon_0 \lambda_0 n_{eff}}, \quad (2.57)$$

where most of the parameters are defined previously and λ_0 is the emission wavelength. In fact, the FOM values for all the 11 designs are also similar. According to Eqn. (2.56) the gain coefficient is inversely proportional to the optical gain spectra width and L_p , however, the variation in the gain coefficient of the 11 designs cannot be well explained by the variation in the

$L_p \cdot \gamma_{32}$ as shown in Fig. 2.41(a), that the correlation between the modal gain coefficient and the inverse of $L_p \cdot \gamma_{32}$ is not satisfactory. Therefore, the gain coefficient cannot be fully accounted for by Eqn. (2.53).

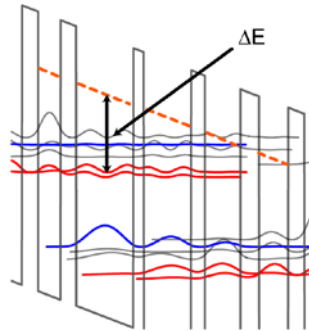


Fig. 2.40 Illustration of the definition of ΔE , the energy difference between the upper laser states (red) and the band edge of the lowest satellite valleys of the quantum well material (orange dashed line).

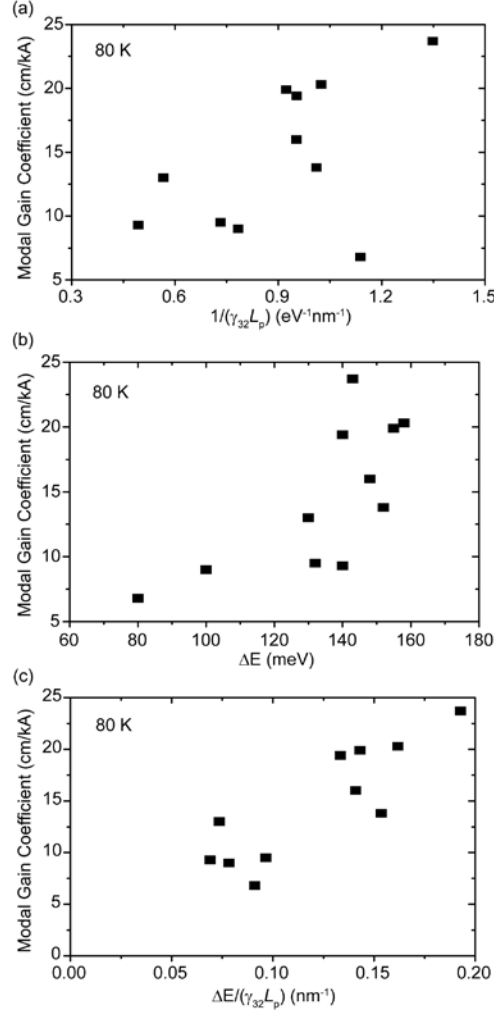


Fig. 2.41 (a) Correlation plot for modal gain coefficient versus $1/(L_p \cdot \gamma_{32})$. (b) Correlation plot for modal gain coefficient versus ΔE . (c) Correlation plot for modal gain coefficient versus $\Delta E/(L_p \cdot \gamma_{32})$.

On the other hand, a clear correlation is found between the modal gain coefficient and ΔE as shown in Fig. 2.41(b), suggesting that scattering of electrons from the injector ground state and/or the upper laser state into the relatively low-lying satellite valleys associated with the highly strained quantum well material may be significant and effectively reduces the electron injection efficiency. If taking into account all three factors: L_p , γ_{32} and ΔE , then a much stronger correlation is found between the modal gain coefficient and $\Delta E/(L_p \cdot \gamma_{32})$ as shown in Fig. 2.41(c). Although it is difficult to know quantitatively the influence of ΔE on the optical gain coefficient from the above correlation plots, they nevertheless provide us with an insight on another important factor that should be taken into account when designing ultra-strong coupling QC lasers.

Apart from further optimizing the band-structure design for these ultra-strong coupling QC lasers, the device performance can also be improved from other aspects such as the waveguide (laser cavity) design. Two of the most important waveguide parameters are the mode confinement factor and the waveguide loss, because both parameters affect the threshold current density, and the waveguide loss also affects the slope efficiency as well as the optical extraction efficiency. The relatively low waveguide loss ($\sim 1.5 \text{ cm}^{-1}$) associated with wafer No. A785 is an important contributing factor to its high performance. Another important waveguide related factor affecting the device performance is the lateral mode profile. In pulsed mode operation, most high performance ultra-strong coupling QC lasers exhibit degradation of the slope efficiency and pulse instability at relatively high output power level. Such changes are usually accompanied by the broadening of the far-field profile in the lateral direction (parallel to the material layers) and sometimes higher order lateral modes are observed (an example is given in Fig. 2.42). These observations indicate that the competition between lateral modes at high power levels is a possible cause for the pulse instability and degradation of slope efficiency, and therefore should be mitigated by optimizing the waveguide design such as employing much narrower waveguide structures to suppress the emergence of higher order lateral modes.

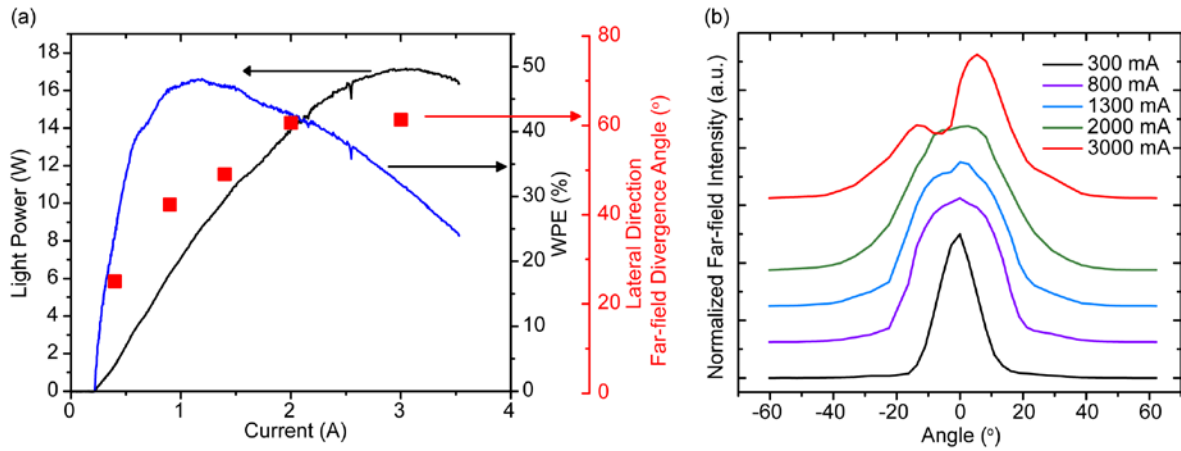


Fig. 2.42 (a) Plot of output optical power, WPE and lateral far-field divergence angle versus input current for one of the highest performance ultra-strong QC lasers (from wafer A785). (b) Lateral far-field profiles at several different input current values for the same laser in (a).

Comprehensive optimizations of the active core as well as the waveguide designs should be employed to further improve the performance of the ultra-strong coupling QC lasers. The coupling strength has been chosen to be $\sim 20 \text{ meV}$ in all of our ultra-strong coupling designs; however, this value is estimated based on some material parameters that have not been directly characterized with high accuracy (such as the interface roughness average height and correlation length), and therefore it may be beneficial to experimentally investigate the optimal coupling strength in a more systematic way. Besides, additional strategies for improving the device temperature characteristic such as those studied in section 2.7 should be properly incorporated in future designs. The energy separation between the upper laser state and the lowest satellite valley

in the active region should also be made sufficiently large to avoid potential current leakage into the satellite valleys. The waveguide structure should also be further optimized to reduce the waveguide loss and improve transverse mode selectivity.

2.9 Summary of the Ultra-strong Coupling QC Lasers

The following two tables provide an overview of the designs and wafers of this study.

Table 1 Summary of the 12 ultra-strong coupling QC designs and some characterization results

Wafer No.	λ (μm)	Sheet doping (cm^{-2})	No. of periods	FWHM (80K) (meV)	FWHM (300K) (meV)	E_{def} 80K (meV)	E_{def} 300K (meV)
A728	4.7	1.00e11	41	32.2	47.3	54.1	57.2
A785	4.6	0.99e11	43	28.6	53.1	51.6	46.7
E109318	4.2	1.04e11	45	37.8	63.1	105.2	109.1
A1015	4.4	1.03e11	43	20.4	45.1	69.0	42.1
A1162	4.7	0.99e11	43	31.8	63.3	107.9	97.4
A1390	5.0	0.98e11	40	41.5	65.7	74.5	114.0
A1392	6.2	0.96e11	50	59.6	82.0	59.1	48.5
M1065	4.0	0.79e11	37	27.7	48.5	155.6	96.5
A1637	4.4	0.73e11	43	38.9	67.4	98.4	102.8
A1639	4.3	0.73e11	43	58.0	71.1	84.9	95.9
A1641	4.9	0.88e11	43	28.3	58.0	86.8	76.4
A1643	5.0	0.88e11	43	31.4	64.8	88.9	89.8

Table 2 Summary of the laser characterization results of the 12 ultra-strong coupling QC designs

Wafer No.	J_{th} (80K) (kA/cm ²)	J_{th} (300K) (kA/cm ²)	T_0 (K)	S (80K) (W/A)	S (300K) (W/A)	Max WPE (80K)	Max WPE (300K)	α_w (80K) (cm ⁻¹)	$g\Gamma$ (80K) (cm/kA)
A728	0.49	2.6	118	5.4	3.6	34.2%	7.9	2.5	16.0
A785	0.40	2.1	125	8.7	5.2	47.3%	15.6	1.5	13.8
E109318	0.60	2.9	114	10.2	2.3	40.0%	3.4	1.8	9.0
A1015	0.27	1.9	105	4.9	3.6	24.0%	10.8	3.5	23.7
A1162	0.62	2.6	130	4.3	2.9	18.1%	5.6	7.7	19.4
A1390	0.37	2.15	112	4.4	2.8	33.6%	9.5	4.6	13.0
A1392	0.58	3.5	107	3.2	1.2	20.6%	2.5	5.3	15.5
M1065	0.70	2.6	145	5.1	2.9	19.1%	5.8	0.6	6.8
A1637	0.89	2.7	152	1.3	2.0	6.0%	3.6	2.0	9.5
A1639	1.1	3.0	181	3.9	3.1	14.2%	5.1	6.8	9.3
A1641	0.57	2.3	133	5.8	3.8	16.9%	6.5	5.4	20.3
A1643	0.57	2.2	163	3.9	4.4	15.7%	8.8	8.8	19.9

List of symbols in Table 1 and Table 2:

λ : average emission wavelength

FWHM: full width at half maximum of the EL spectra

E_{def} : energy defect

J_{th} : threshold current density

T_0 : characteristic temperature

S: slope efficiency

α_w : waveguide loss

$g\Gamma$: modal gain coefficient

3. Importance of interface roughness induced intersubband scattering in mid-infrared Quantum Cascade lasers

Since QC lasers are semiconductor lasers based on intersubband transitions in quantum wells, one of the most important parameters in QC laser performance is the relation between the lifetimes of the upper and lower laser subbands, which determines the magnitude of population inversion. Therefore, it is crucial to accurately account for intersubband scattering when designing QC lasers.

The intersubband transition lifetimes can be determined by various scattering processes such as longitudinal optical (LO) phonons, longitudinal acoustic optical (LA) phonons, alloy disorder, or ionized impurities. [34,35] Traditionally, since LO-phonons have the fastest scattering rate among those, intersubband scattering in QC lasers is understood to be dominated by LO-phonon scattering. What has long been neglected but is more recently reconsidered [36] is that interface roughness also causes intersubband scattering.[37] Interface roughness induced scattering has been shown to have effects on the intersubband absorption, [38] the temperature dependent intersubband broadening [37] and the transport process limited by resonant tunneling,[39] all of which strongly affect the QC laser performance. Recently, it has been shown that the calculated interface roughness (IFR) scattering lifetimes between the upper and lower laser states, depending on the interface conditions, can be comparable to or even faster than those caused by LO-phonon scattering.[40] However, a thorough experimental study of the effect of interface roughness on intersubband scattering lifetimes is still lacking.

Here, we calculate the upper and lower laser level lifetimes of 22 existing QC laser designs with and without the consideration of IFR scattering. Assuming the same interface roughness conditions for all designs, the calculated lifetimes' dependence on IFR scattering may vary depending on different lasing wavelength and material compositions as well as design, i.e. wave function overlap with interfaces. We then measure the non-lasing current and voltage (IV) characteristic curves for 14 of these QC devices which are directly available. Since the maximum current density is limited by the upper laser level lifetime,[41] a comparison with the calculations can be made. A significantly better agreement between the experimental results and the calculations is determined when IFR scattering is taken into account which confirms that IFR scattering plays an important role in intersubband scattering in QC lasers.

Interface roughness can be modeled as a random profile with Gaussian autocorrelation which is characterized by an average root-mean-square step height Δ and an in-plane correlation length λ . The intersubband scattering lifetime (τ_{IFR}) caused by interface roughness can then be calculated: [37]

$$\hbar\tau_{IFR}^{-1} = \frac{\pi m^*}{\hbar^2} \Delta^2 \Lambda^2 \delta U^2 \sum_i \{f_2(z_i) f_1(z_i)\}^2 e^{-\frac{\Lambda^2 q_{21}^2}{4}} \quad (3.1)$$

Here, δU is the band offset, $f_2(z_i)$ and $f_1(z_i)$ are the wave function amplitudes at the i th interface, and q_{21} is the absolute value of the two-dimensional scattering vector in this process.[42] Figure 3.1 shows the band structure of a QC laser with the parabolas representing the energy dispersion for upper (subband 2) and lower (subband 1) laser levels. The arrow q_{21} illustrates the interface roughness induced transition from subband 2 to subband 1. A constant Δ

~ 0.15 nm which is about half of the monolayer thickness and a $\lambda \sim 6$ nm are used for all the designs analyzed in the following interface roughness scattering calculations.[43]

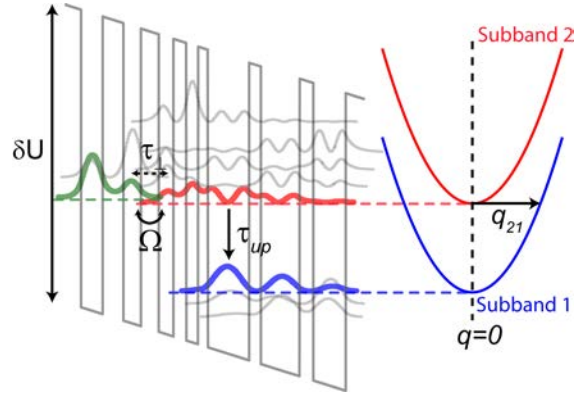


Fig. 3.1 Typical band structure of a QC laser with upper laser level in red, lower laser level in blue and injector state in green. The parabolas represent the energy dispersion for each subbands with the arrow indicating the interface roughness induced transition from the upper to lower laser levels.

The upper and lower laser level lifetimes of 22 existing QC laser designs, [44–54] some from our research group and some from literature, are calculated and shown in Fig. 3.2 (a) and (b) respectively. The lifetimes are first calculated in two different ways: LO-phonon scattering (red circles) and IFR scattering (black squares) separately. As seen in Fig. 3.2, the lifetimes calculated from IFR scattering (τ_{IFR}) are comparable to the lifetimes calculated from LO-phonon scattering (τ_{LO}), this means that the effect of IFR scattering on intersubband scattering can no longer be neglected, and both LO-phonon and IFR scattering processes should be taken into account in calculating the overall intersubband lifetimes. Combining both scattering processes, τ_{total} can be calculated by $1/\tau_{\text{total}} = 1/\tau_{\text{LO}} + 1/\tau_{\text{IFR}}$ and is shown as blue triangles in Fig.3.2.

For the upper laser level lifetimes, since the square of q_{21} in Eq. (3.1) is proportional to the transition energy between two states, the calculated τ_{IFR} thus has an exponential dependence on the transition energy: the longer the wavelength, the shorter the τ_{IFR} is. While LO-phonon scattering rate is just quadratically dependent on the scattering vector,[34] IFR scattering has become the dominating intersubband scattering mechanism for the longer wavelength ($>8\mu\text{m}$) QC lasers as shown in Fig. 3.2 (a). Even though LO-phonon scattering still dominates at the shorter wavelength range ($\sim 4\mu\text{m}$), the calculated τ_{total} is reduced by almost 50% when including IFR scattering. Plotting the calculated τ_{total} as a function of lasing wavelength, the dependence of upper laser level lifetimes on the wavelength is clearly seen in Fig.3.3.

On the other hand, the conventional depopulation energy for the lower laser level is designed to be around 34 meV for the QC laser designs we analyze here, so the difference between τ_{IFR} of the lower laser level has very little dependence on the depopulation energy. However, the material compositions for different wavelength range designs are different, thus affecting the band offset δU in Eq. (3.1). For QC lasers with design wavelength $>8\mu\text{m}$, lattice-matched $\text{In}_{0.53}\text{Ga}_{0.47}\text{As}/\text{Al}_{0.48}\text{In}_{0.52}\text{As}$ on InP is used; for QC lasers with $<8\mu\text{m}$ design wavelength, strain-balanced material is used to create a larger band offset. The larger band offset

for short wavelength QC laser designs results in the domination of the lower laser level lifetime by IFR scattering as can be seen in Fig.3.2 (b).

Quantum Cascade lasers are usually designed to have a sufficiently quick electron injection from the preceding injector to the upper laser level through resonant tunneling (see

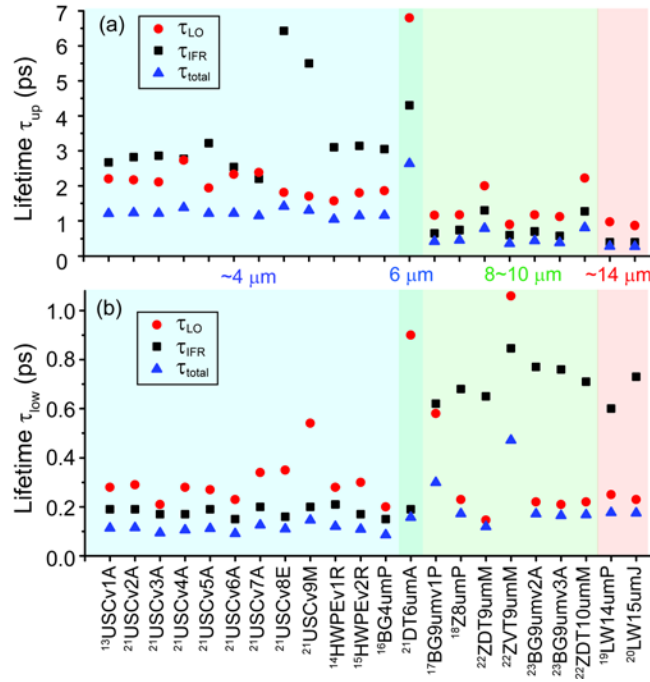


Fig. 3.2 (a) Upper laser level lifetimes and (b) lower laser level lifetimes calculated for different QC laser designs. Black squares are lifetimes calculated by IFR scattering only. Red circles are lifetimes calculated by LO phonon scattering only. Blue triangles are lifetimes taking into account of both IFR and LO phonon scattering. Different color shaded area represent different lasing wavelength regions.

Fig.3.1), and electrons depopulate similarly fast from the lower laser level to the following injector. In the tight-binding approximation, the current density can be written as in Ref. 41 :

$$J = qN_s \frac{2\Omega^2\tau_{\perp}}{1+\Delta^2\tau_{\perp}^2+4\Omega^2\tau_{up}\tau_{\perp}} \quad (3.2)$$

where q is the electric charge, N_s is the sheet doping density, Ω is the coupling strength between the injector ground state and the upper laser level, $\hbar\Delta$ is the energy detuning from resonance, τ_{\perp} is the in-plane momentum relaxation time, and τ_{up} is the upper laser level lifetime. When the system is at full resonance ($2\hbar\Delta = 0$) and the coupling energy between the injector ground state and the upper laser level is strong enough ($4\Omega^2\tau_{up}\tau_{\perp} \gg 1$), which is the case for most of the designs analyzed here, the maximum current density (J_{max}) can be conveniently

written as $J = qN_s \tau_{transit}$ and $\tau_{transit} = 2\tau_{up}$. Here $\tau_{transit}$ is defined as the global transit time of the electron across a period of the active region at resonance.[55]

The current-voltage characteristics of 14 non-lasing circular mesa samples from the QC laser designs in Fig.3.1 are measured.[44, 47-50, 51-54] As the applied voltage keeps increasing, the QC device eventually encounters the cut-off voltage (V_{cutoff}) at which the ground state in the injector is no longer aligned with the upper laser level, forming a kink in the IV and the

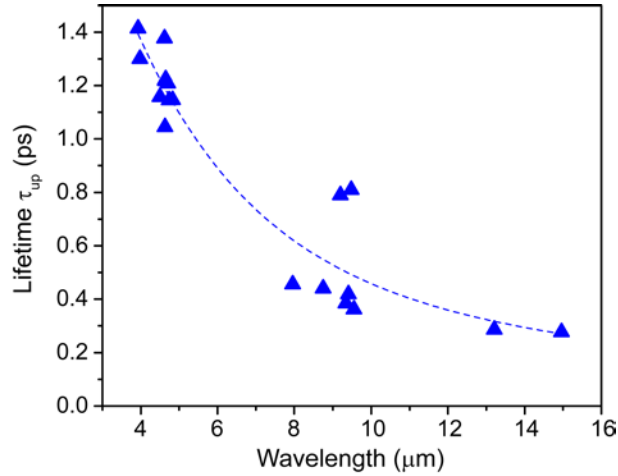


Fig. 3.3 Calculated upper laser level lifetimes when both LO-phonon and IFR scattering are taken into account as a function of wavelength. The dashed line is a guide for the eye only.

differential resistance deviates from the original value. The J_{max} of a QC device is determined as shown in Fig.3.4. The inset in Fig.3.4 shows the light-current-voltage characteristics of the laser fabricated from the same QC wafer. The cut-off voltage is the same for both the lasing and non-lasing QC devices though J_{max} increases for a laser device due to the reduction of differential resistance when there is stimulated emission. With J_{max} for all 14 QC designs determined and using N_s of each design, $\tau_{transit}$ can be extracted. The measured $\tau_{transit}$ are plotted in Fig.3.5 as a function of lasing wavelength. A similar dependence on the lasing wavelength for the measured $\tau_{transit}$ is also seen as in the case for the calculated τ_{up} (Fig.3.3).

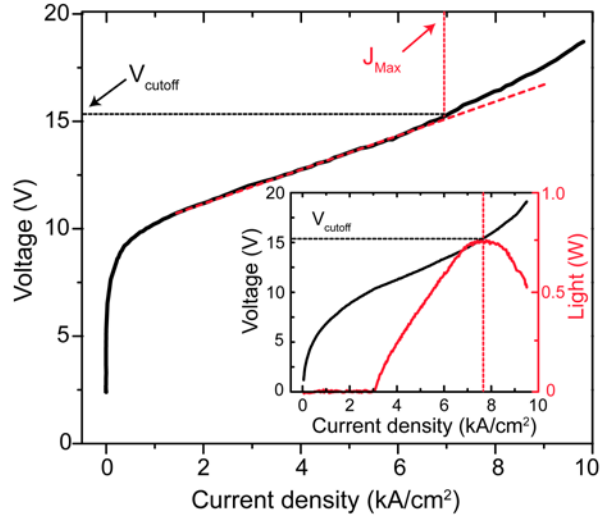


Fig. 3.4 Current-voltage characteristic of a non-lasing circular mesa sample at $T=80$ K. The inset shows the light-current-voltage characteristic of a laser fabricated from the same wafer.

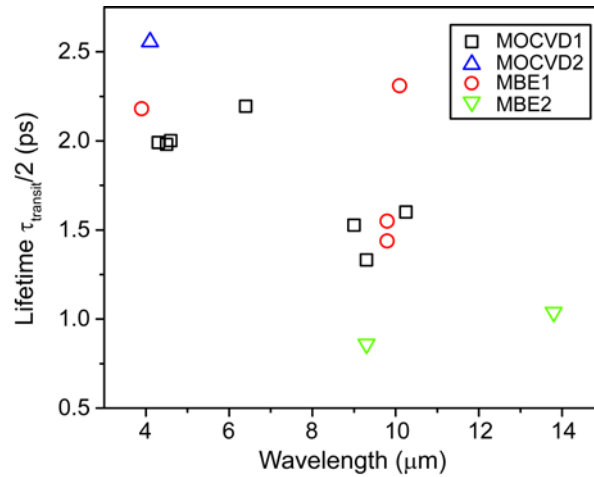


Fig. 3.5 Measured transit lifetimes as a function of the lasing wavelength. Different shapes (colors) indicate different growth facilities and growth techniques.

A direct comparison between the measurements and the calculations can be made from the relationship between τ_{up} and τ_{transit} derived above. However, the actual doping density may be slightly different from the designed values due to different growth conditions. Also, the model [41] used to derive Eq. (3.2) underestimates electron transport through many injector states, it is more suitable to set upper laser level lifetime as the lower limit for half of the transit lifetime. [56] Therefore, instead of comparing the measured $\tau_{\text{transit}}/2$ values directly with the calculated τ_{up} values, we plot the calculated τ_{up} as a function of the measured $\tau_{\text{transit}}/2$ to illustrate the correlation between them. As shown in Fig.3.6, the τ_{up} calculated using LO-phonon scattering only are plotted as red circles, the linear fit through all the data points has a slope of 0.43, standard error 0.27 and correlation coefficient of 0.43; the τ_{up} calculated with both LO-phonon and IFR scattering are plotted as blue triangles, the linear fit through all the data point has a slope

of 0.66, standard error 0.15 and correlation coefficient 0.79. The much smaller error and the larger correlation coefficient indicate a better agreement between the measured τ_{transit} and the calculated τ_{up} when IFR scattering is taken into account, which confirms that IFR scattering plays a non-negligible role for intersubband scattering in mid-IR QC lasers.

In conclusion, theoretical calculations of both upper and lower laser level lifetimes for many existing mid-IR QC laser designs have been demonstrated with and without the consideration of IFR scattering. The upper laser level lifetime is reduced by almost a factor of 2 when not only LO-phonon but also IFR scattering is taken into account; meanwhile, the calculated lower laser level lifetimes show a dependence on material compositions and the larger band offset results in the domination of lower laser level lifetime by IFR scattering. The importance of the calculated total upper laser level lifetime τ_{up} on lasing wavelength due to the energy of the transition in IFR induced intersubband scattering is also observed in the measured τ_{transit} : the longer the wavelength, the smaller the τ_{up} or τ_{transit} are. Linear relationships with slopes of 0.43 ± 0.27 and 0.66 ± 0.15 ; correlation coefficients of 0.79 and 0.43, with and without the consideration of IFR scattering respectively, have been established between the measurement and the calculation. The significantly better correlation when both LO-phonon and IFR scattering are taken into account not only proves the importance of including IFR scattering into the evaluation of intersubband scattering lifetime in mid-IR QC laser designs but opens the exciting possibility of using interface roughness scattering to engineer lifetimes for improved laser performance.

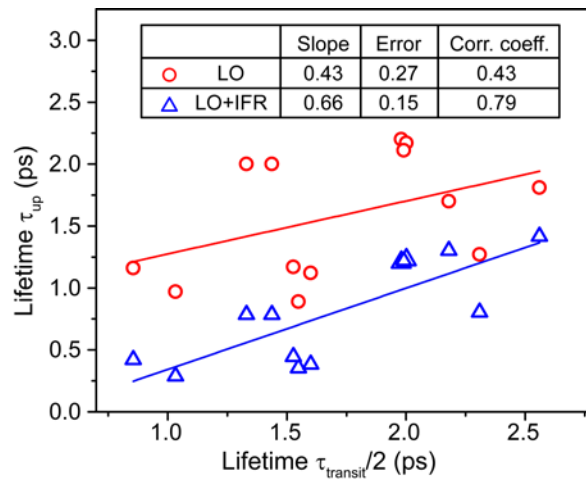


Fig. 3.6 Blue triangles and red circles are the calculated upper laser level lifetimes plotted as a function of half the measured transit lifetimes with and without taking into account of interface roughness scattering, respectively. The lines are linear fits through the data points. The inset table lists the slopes, standard error and correlation coefficients of the fit curves.

References

- [1] A. Bismuto, R. Terazzi, B. Hinkov, M. Beck, and J. Faist, "Fully automatized quantum cascade laser design by genetic optimization," *Applied Physics Letters* **101**, 021103 (2012).
- [2] J. D. Kirch, J. C. Shin, C.-C. Chang, L. J. Mawst, D. Botez and T. Earles, "Tapered active-region quantum cascade lasers ($\lambda \approx 4.8 \mu\text{m}$) for virtual suppression of carrier-leakage currents," *Electronic Letters* **48**, 234-235 (2012).
- [3] M. Yamanishi, K. Fujita, T. Edamura, and H. Kan, "Indirect pump scheme for quantum cascade lasers: dynamics of electron-transport and very high T_0 -values," *Optics Express* **16**, 20748-20758 (2008).
- [4] T. Gresch, M. Giovannini, N. Hoyer, and J. Faist, "Quantum Cascade Lasers With Large Optical Waveguides," *IEEE Photonics Technology Letters* **18**, 544-546 (2006).
- [5] Y. Bai, N. Bandyopadhyay, S. Tsao, E. Selcuk, S. Slivken, and M. Razeghi, "Highly temperature insensitive quantum cascade lasers," *Applied Physics Letters* **97**, 251104 (2010).
- [6] J. Faist, "Wallplug efficiency of quantum cascade lasers: Critical parameters and fundamental limits," *Applied Physics Letters* **90**, 253512 (2007).
- [7] Q. K. Yang, C. Schilling, R. Ostendorf, S. Hugger, F. Fuchs, and J. Wagner, "Wall-plug efficiency of mid-infrared quantum cascade lasers," *Journal of Applied Physics* **111**, 053111 (2012).
- [8] M. D. Escarra, A. J. Hoffman, K. J. Franz, S. S. Howard, R. Cendejas, X. Wang, J.-Y. Fan, and C. Gmachl, "Quantum cascade lasers with voltage defect of less than one longitudinal optical phonon energy," *Applied Physics Letters* **94**, 251114 (2009).
- [9] Y. Bai, S. Slivken, S. R. Darvish, and M. Razeghi, "Room temperature continuous wave operation of quantum cascade lasers with 12.5% wall plug efficiency," *Applied Physics Letters* **93**, 021103 (2008).
- [10] R. Ferreira, and G. Bastard, "Evaluation of some scattering times for electrons in unbiased and biased single- and multiple-quantum-well structures," *Physical Review B* **40**, 1074-1086 (1989).
- [11] T. Unuma, T. Takahashi, T. Noda, M. Yoshita, H. Sakaki, M. Baba, and H. Akiyama, "Effects of interface roughness and phonon scattering on intersubband absorption linewidth in a GaAs quantum well," *Applied Physics Letters* **78**, 3448-3450 (2001).
- [12] C. Sirtori, F. Capasso, J. Faist, A. L. Hutchinson, D. L. Sivco, and A. Y. Cho, "Resonant Tunneling in Quantum Cascade Lasers," *IEEE Journal of Quantum Electronics* **34**, 1722-1729 (1998).
- [13] J. B. Khurgin, "Inhomogeneous origin of the interface roughness broadening of intersubband transitions," *Applied Physics Letters* **93**, 091104 (2008).

- [14] A. Bismuto, R. Terazzi, M. Beck, and J. Faist, "Influence of the growth temperature on the performances of strain-balanced quantum cascade lasers," *Applied Physics Letters* **98**, 091105 (2011).
- [15] Y. Chiu, Y. Dikmelik, P. Q. Liu, N. L. Aung, J. B. Khurgin, and C. F. Gmachl, "Importance of interface roughness induced intersubband scattering in mid-infrared quantum cascade lasers," *Applied Physics Letters*, accepted.
- [16] K. J. Franz, P. Q. Liu, J. J. J. Raftery, M. D. Escarra, A. J. Hoffman, S. S. Howard, Y. Yao, Y. Dikmelik, X. Wang, J.-Y. Fan, J. B. Khurgin, and C. Gmachl, "Short Injector Quantum Cascade Lasers," *IEEE Journal of Quantum Electronics* **46**, 591-600 (2009).
- [17] M. C. Wanke, F. Capasso, C. Gmachl, A. Tredicucci, D. L. Sivco, A. L. Hutchinson, S.-N. G. Chu, and A. Y. Cho, "Injectorless quantum-cascade lasers," *Applied Physics Letters* **78**, 3950-3952 (2001).
- [18] S. Katz, A. Vizbaras, G. Boehm, and M.-C. Amann, "High-performance injectorless quantum cascade lasers emitting below 6 μm ," *Applied Physics Letters* **94**, 151106 (2009).
- [19] R. W. Boyd, *Nonlinear Optics*, Academic Press (1992).
- [20] J. B. Khurgin, Y. Dikmelik, P. Q. Liu, A. J. Hoffman, M. D. Escarra, K. J. Franz, and C. F. Gmachl, "Role of interface roughness in the transport and lasing characteristics of quantum-cascade lasers," *Applied Physics Letters* **94**, 091101 (2009).
- [21] H. Callebaut, and Q. Hu, "Importance of coherence for electron transport in terahertz quantum cascade lasers," *Journal of Applied Physics* **98**, 104505 (2005).
- [22] R. Terazzi, and J. Faist, "A density matrix model of transport and radiation in quantum cascade lasers," *New Journal of Physics* **12**, 033045 (2010).
- [23] E. Dupont, S. Fatholouloumi, and H. C. Liu, "Simplified density-matrix model applied to three-well terahertz quantum cascade lasers," *Physical Review B* **81**, 205311 (2010).
- [24] S. Tsujino, A. Borak, E. Müller, M. Scheinert, C. V. Falub, H. Sigg, D. Grützmacher, M. Giovannini, and J. Faist, "Interface-roughness-induced broadening of intersubband electroluminescence in p-SiGe and n-GaInAs/AlInAs quantum-cascade structures," *Applied Physics Letters* **86**, 062113 (2005).
- [25] A. Wittmann, Y. Bonetti, J. Faist, E. Gini, and M. Giovannini, "Intersubband linewidths in quantum cascade laser designs," *Applied Physics Letters* **93**, 141103 (2008).
- [26] P. Offermans, P. M. Koenraad, J. H. Wolter, M. Beck, T. Aellen, and J. Faist, "Digital alloy interface grading of an InAlAs/InGaAs quantum cascade laser structure studied by cross-sectional scanning tunneling microscopy," *Applied Physics Letters* **83**, 4131-4133 (2003).
- [27] P. Q. Liu, A. J. Hoffman, M. D. Escarra, K. J. Franz, J. B. Khurgin, Y. Dikmelik, X. Wang, J.-Y. Fan, and C. F. Gmachl, "Highly Power-efficient Quantum Cascade Lasers," *Nature Photonics* **4**, 95-98 (2010).

- [28] J. Faist, D. Hofstetter, M. Beck, T. Aellen, M. Rochat, and S. Blaser, “Bound-to-continuum and two-phonon resonance quantum-cascade lasers for high duty cycle, high-temperature operation,” *IEEE Journal of Quantum Electronics* **38**, 533–546 (2002).
- [29] Y. Yao, W. O. Charles, T. Tsai, J. Chen, G. Wysocki, and C. F. Gmachl, “Broadband quantum cascade laser gain medium based on a “continuum-to-bound” active region design,” *Applied Physics Letters* **96**, 211106 (2010).
- [30] Y. Yao, X. Wang, J. Fan, and C. F. Gmachl, “High performance “continuum-to-continuum” quantum cascade lasers with a broad gain bandwidth of over 400 cm^{-1} ,” *Applied Physics Letters* **97**, 081115 (2010).
- [31] K. Fujita, S. Furuta, T. Dougakiuchi, A. Sugiyama, T. Edamura, and M. Yamanishi, “Broad-gain ($\Delta\lambda/\lambda_0 \sim 0.4$), temperature-insensitive ($T_0 \sim 510\text{K}$) quantum cascade lasers,” *Optics Express* **19**, 2694-2701 (2011).
- [32] Q. K. Yang, C. Mann, F. Fuchs, R. Kiefer, K. Koehler, N. Rollbuehler, H. Schneider, and J. Wagner, “Improvement of $\lambda \approx 5 \mu\text{m}$ quantum cascade lasers by blocking barriers in the active regions,” *Applied Physics Letters* **80**, 2048-2050 (2002).
- [33] J. C. Shin, M. D’Souza, Z. Liu, J. Kirch, L. J. Mawst, D. Botez, I. Vurgaftman, and J. R. Meyer, “Highly temperature insensitive, deep-well 4.8 μm emitting quantum cascade semiconductor lasers,” *Applied Physics Letters* **94**, 201103 (2009).
- [34] R. Ferreira and G. Bastard, *Phys. Rev. B*, **40**, 1074 (1989).
- [35] T. Unuma, M. Yoshita, T. Noda, H. Sakaki, and H. Akiyama, *J. Appl. Phys.*, **93**, 1586 (2003).
- [36] M. P. Semtsiv, Y. Flores, M. Chashnikova, G. Monastyrskyi, and W. T. Masselink, *Appl. Phys. Lett.*, **100**, 163502 (2012).
- [37] T. Unuma, T. Takahashi, T. Noda, M. Yoshita, H. Sakaki, M. Baba, and H. Akiyama, *Appl. Phys. Lett.*, **78**, 3448 (2001).
- [38] K. L. Campman, H. Schmidt, A. Imamoglu, and A. C. Gossard, *Appl. Phys. Lett.*, **69**, 2554 (1996).
- [39] J. B. Khurgin, Y. Dikmelik, P. Q. Liu, A. J. Hoffman, M. D. Escarra, K. J. Franz, and C. F. Gmachl, *Appl. Phys. Lett.*, **94**, 091101 (2009).
- [40] A. Bismuto, R. Terazzi, M. Beck, and J. Faist, *Appl. Phys. Lett.*, **98**, 091105 (2011).
- [41] C. Sirtori, F. Capasso, J. Faist, A. Hutchinson, D. Sivco, and A. Cho, *IEEE J. Quantum Electron.*, **34**, 1722 (1998).
- [42] J. B. Khurgin, *Appl. Phys. Lett.*, **93**, 091104 (2008).

- [43] P. Offermans, P. L. Koenraad, J. H. Wolter, M. Beck, T. Aellen, J. Faist, *Appl. Phys. Lett.*, 83, pp. 4131-4133 (2003).
- [44] P. Q. Liu, A. J. Hoffman, M. D. Escarra, K. J. Franz, J. B. Khurgin, Y. Dikmelik, X. Wang, J.Y. Fan, and C. F. Gmachl, *Nature Photonics*, 4, 95-98 (2010).
- [45] A. Evans, S. R. Darvish, S. Slivken, J. Nguyen, Y. Bai, M. Razeghi, *Appl. Phys. Lett.*, 91, 071101 (2007).
- [46] Y. Bai, S. Slivken, S. Kuboya, S. R. Darvish, and M. Razeghi, *Nature Photonics*, 4, 99-102 (2010).
- [47] Y. Yao, X. Wang, J.Y. Fan, and C. F. Gmachl, *Appl. Phys. Lett.*, 97, 081115 (2010).
- [48] Y. Yao, W. O. Charles, T. Tsai, J. Chen, G. Wysocki, and C. F. Gmachl, *Appl. Phys. Lett.*, 96, 211106 (2010).
- [49] Z. Liu, D. Wasserman, S. S. Howard, A. J. Hoffman, C. F. Gmachl, X. Wang, T. Tanbun-Ek, L. Cheng, and F.S. Choa, *IEEE PTL.*, 18, 12, 1347-1349 (2006).
- [50] X. Huang, W. O. Charles, and C. F. Gmachl, *Opt. Express*, 19, 8297-8302 (2011).
- [51] K. Fujita, M. Yamanishi, T. Edamura, A. Sugiyama, and S. Furuta, *Appl. Phys. Lett.*, 97, 201109 (2010).
- [52] USCv2A, USCv3A, USCv4A, USCv5A, USCv6A, USCv7A, USCv8E, USCv9M, and DT6umA are ultra-strong coupling Quantum Cascade laser designs lasing at ~ 4 to $6 \mu\text{m}$, similar to the USCv1A design as in Ref. 13.
- [53] ZD9TumM, ZVT9umM, and ZDT10umM are 8 to $10 \mu\text{m}$ Quantum Cascade laser designs similar to the Z8umP design as in Ref. 18.
- [54] BG9umv2A and BG9umv3A are broad gain Quantum Cascade laser designs similar to the designs in Ref. 16 and 17 lasing at $\sim 9 \mu\text{m}$.
- [55] J. Faist, *Appl. Phys. Lett.*, 90, 253512 (2007).
- [56] J. B. Khurgin, Y. Dikmelik, *Opt. Eng.*, 49(11),111110 (2010).